UNIVERSITY OF TARTU

FACULTY OF SCIENCE AND TECHNOLOGY

INSTITUTE OF CHEMISTRY

The Impact of a Temperature-Sensitive Sensor on a Commercial Li-ion Battery Cell Graphite Electrode

Annabel Olgo

Master's thesis (30 ECTs)

Chemistry

Supervisors: Rasmus Palm, Ph.D

Quentin Jacquet, Ph.D

Sandrine Lyonnard, Ph.D

Tartu 2023

Information sheet

Temperatuuritundliku sensori mõju kommertsiaalse Li-ioon aku grafiitelektroodile

Töös uuriti temperatuuritundliku optilise fiibri mõju Li-ioonide interkaleerumisele kommetriaalse Li-ioon aku grafiitelektroodi. Kommertsiaalse Li-ioon aku, kuhu oli lisatud temperatuuritundlik sensor ja võrdluselektrood, karakteriseerimiseks kasutati *operando* WAXS meetodit Euroopa sünkrotronkiirguse uurimise keskuses. Tulemustest selgus, et optilise fiibri sisestamine kommertsiaalsesse Li-ioon mõjutab lokaalset Li-ioonide kineetikat ja sellest tulenevalt ka Li_xC_6 faaside moodustumist.

Märksõnad: Liitiumioonaku, Li-ioonide interkaleerumine grafiitelektroodi, sensor, grafiitelektrood, *operando* WAXS

CERCS koodid: P250 Tahke aine: struktuur, termilised ja mehhaanilised omadused, kristallograafia, faaside tasakaal, P401 Elektrokeemia, T140 energeetika

The Impact of a Temperature-Sensitive Sensor on a Commercial Li-ion Battery Cell Graphite Electrode

This thesis aims to provide insight into structural changes and lithiation of the graphite electrode of a commercial multi-layered prismatic pouch cell. The commercial pouch cell was equipped with a reference electrode and temperature-sensitive optical fiber and (dis)charged at various current rates. The data analysed in this thesis was collected during the *operando* wide-angle X-ray scattering experiment conducted as a part of the INSTABAT and BIGMAP projects. It was observed that the presence of the fiber causes heterogeneities in the state of charge around the optical fiber. The results demonstrate that the information on the state of charge obtained near the optical fiber exclusively describes the region around the optical fiber.

Keywords: Lithium-ion battery, graphite lithiation, sensor, graphite electrode, *operando* WAXS

CERCS codes: P250 Condensed matter: structure, thermal and mechanical properties, crystallography, phase equilibria, P401 Electrochemistry, T140 energy research

Table of Contents

Introduction

Lithium-ion batteries are one of the leading technologies in modern energy storage solutions because of their compact size, high energy density, and long lifetime [1]. In recent years, their importance as high-performance energy storage devices has become more significant [2] in terms of reducing carbon emissions [3] and increasing demand for cleaner energy sources [4]. Addressing climate change concerns has accelerated advancements in battery technology, driving researchers to explore novel materials, battery systems, and strategies for enhancing their performance, safety, and sustainability. One way to improve lithium-ion batteries' performance, safety, and lifetime is to integrate smart sensing technology (sensors) into a battery cell [5]. These sensors enable the measurement of characteristic parameters of a battery cell and estimate the state of health and charge of the battery. State of health (SoH) describes the evolution of crucial cell parameters such as internal resistance, cell voltage, and self-discharge rate. It is used as a quantitive indicator of the battery's health [6]. The state of charge (SoC) expresses a battery cell's remaining dischargeable capacity. SoH and SoC are compared to the initial states obtained at the beginning of a battery's life [6,7]. As a battery undergoes cycling, its electrochemical performance deteriorates, leading to diminished SoH and SoC. However, by monitoring crucial cell parameters in real-time and correlating them with the physicochemical degradation of battery components, it is possible to enhance safety and lifetime by triggering self-healing processes or optimizing working conditions [5]. Nonetheless, for accurate estimations of SoH and SoC of a battery and physicochemical degradation, the data obtained with a sensor has to be reliable. One way to control the reliability of a sensor is to study structural changes in electrodes while a battery is operating.

This work aims to provide insight into whether correlating structural changes in the graphite electrode with data obtained with a sensor is a reliable way to describe the SoH and SoC of a battery cell. An *operando* synchrotron wide-angle X-ray scattering experiment was conducted in collaboration with BIG-MAP and INSTABAT projects to study a commercial prismatic lithium-ion battery pouch cell. The battery cell was equipped with two sensors – a reference electrode to monitor electrode potentials and a temperature-sensitive sensor for measuring temperature changes inside a battery cell while cycling at low and high C-rates. This work focuses on two main aspects: 1) analysing structural changes and lithiation of the graphite electrode within the commercial cell, and 2) examining the impact of the presence of a temperature-sensitive sensor on the local lithiation mechanism and kinetics.

1. Literature Overview

1.1 Basic Working Principle of Secondary Batteries

Batteries are devices that convert chemical energy into electrical energy via spontaneous electrochemical reactions. Typically, a battery contains several electrochemical cells; each cell consists of an electrolyte, a separator, and two electrodes – one positive and one negative. The electrodes are connected by an external load and are separated by a separator. The separator prevents the migration of electrons within the electrochemical cell. The electrodes and the separator are in contact with an electrolyte (Figure 1). The electrolyte acts as an ion-conducting medium, enabling the transfer of ions from the negative electrode to the positive electrode and vice versa [8].

Batteries can be categorized based on numerous characteristics, such as the reversibility of reactions, type of electrolyte, and specific applications. Typically, batteries have been divided into primary and secondary (rechargeable) batteries. The fundamental difference between these two types is that in primary batteries electrochemical reactions are irreversible, but in rechargeable batteries, they can be reversed by applying a positive current (charging) [9]. The applied charging (C) or discharging (D) current is typically expressed as a C(D)-rate – 1C(D) corresponds to the current required to charge or discharge the battery in one hour [8].

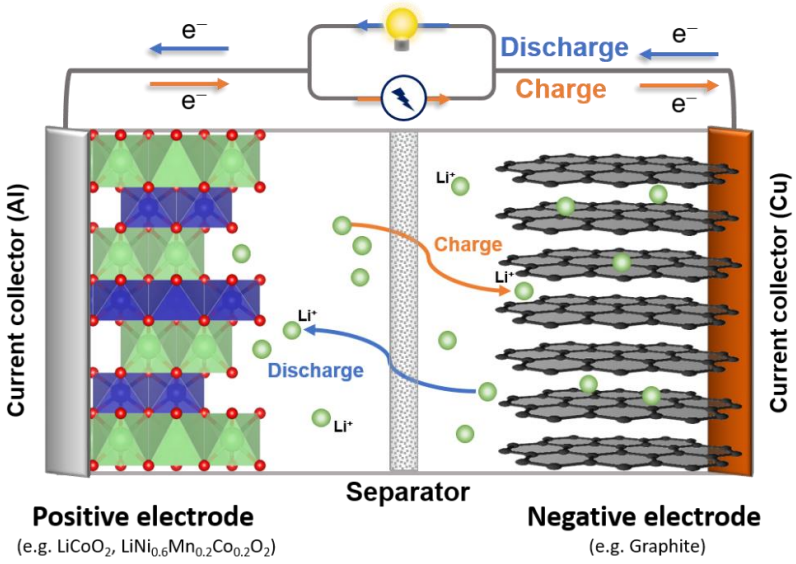

Figure 1. Schematic illustration of the working principle of a lithium-ion battery cell.

In the context of Li-ion batteries (LIBs), graphite is commonly used as the negative electrode and layered oxides (e.g., $LiCoO_2$, $LiN_{0.6}Mn_{0.2}Co_{0.2}O_2$) as the positive electrode materials. During the charging process, when a positive current is applied, electrons move from the positive electrode to the negative electrode via an external circuit. This leads to the oxidation

of the positive electrode and the reduction of the negative electrode (Equations 1.1 and 1.2). In order to maintain electroneutrality, Li-ions are released from the positive electrode and migrate through the electrolyte to the negative electrode. Once at the graphite surface, Li-ions intercalate into interlayer spaces in graphite, forming intercalation compounds (Li_xC_6, $0 < x < 1$). The additional energy gained from an applied current is stored in chemical bonds between Li-ions and carbon atoms [8].

Positive electrode: $$LiMO_2 \rightleftarrows Li_{1-x}MO_2 + xLi^+ + xe^- \quad (1.1)$$

Negative electrode: $$xLi^+ + xe^- + C_6 \rightleftarrows Li_XC_6 \quad (1.2)$$

The opposite process, known as discharging, involves breaking the chemical bonds between Li-ions and carbon atoms and deintercalation of Li-ions from the negative electrode, resulting in released energy. The negative electrode is oxidized during discharging, and the positive electrode is reduced.

1.2 Lithium-Ion Batteries

Nowadays, lithium-ion batteries (LIBs) are the leading technology in the battery industry. LIBs have been widely used in portable devices, electric vehicles, and large-scale energy storage due to their high energy density, high operating voltage, and long cycling lifetime [10]. LIBs owe their excellent electrochemical performance to the low molar mass (M_{Li} = 6.94 g mol^{-1}) [11] and highly negative reduction potential (E = –3.045 V *vs.* SHE) of lithium [9].

Due to lithium's electrochemical and atomic properties, LIBs have dominated the battery industry for over 30 years. However, the breakthrough of LIBs was only possible because of the discovery of a suitable and stable cathode material. In 1980, Goodenough *et al.* introduced $LiCoO_2$ as a new promising positive electrode material for LIBs [12]. The new positive electrode material had a high theoretical capacity of 274 mAh g^{-1} and demonstrated a practical capacity of 140 mAh g^{-1} at E = 4.2 V *vs*. Li$^+$/Li. This accelerated the research and development of LIBs. In 1991, Sony released the first commercial LIB, using $LiCoO_2$ as a positive electrode material with graphite as a negative electrode material [13].

Despite their impressive electrochemical performance and dominance in the battery industry, there are numerous issues regarding electrochemical performance, cell components, and safety. Battery safety and electrochemical performance depend highly on battery chemistry and electrode materials. For example, graphite is the choice of negative electrode material for LIBs because it can intercalate Li-ions at a low potential (E < 0.1 V *vs.* Li$^+$/Li), which is close to the

reduction potential of lithium. Low intercalation potential increases the cell's voltage range and, therefore, energy density. However, the low intercalation potential is close to the reduction potential of lithium, where Li^+ is reduced to its metallic form, which is one of the main reasons for metallic lithium deposition on the negative electrode [14,15]. During cycling, additional metallic lithium deposes on the graphite electrode, leading to the formation of dendrites. Dendrites can penetrate the separator, causing short circuits and, therefore, internal failure of a battery. Moreover, the deposited metallic lithium is highly reactive, initiating parasitic reactions between the electrode materials and the electrolyte [16]. These parasitic reactions increase the internal temperature and gas evolution inside a battery, resulting in a thermal runaway [17].

To address these, numerous strategies have been proposed, ranging from designing novel electrolytes and electrode materials to monitor the state of health (SoH) and charge (SoC) of a battery to improve the safety, lifetime, and electrochemical performance of LIBs [18–20].

1.3 Smart Batteries and Smart Sensing Technology

The objective of a smart battery is to increase performance, lifetime, and safety by using integrated sensors inside or outside of a battery cell to monitor key parameters such as temperature, electrode potential, current, pressure, gas concentration, etc. By measuring these key parameters in real-time, it is possible to improve the SoH and SoC [21]. The measured data on the key parameters are forwarded and continuously analysed by a control system. The control system determines actions to ensure a battery's safety and optimized performance. For example, it manages charging and discharging rates, protects against overheating, and triggers a self-healing process if needed. The analysed data and information are forwarded to a monitoring device through the communication interface [20].

To promote the development and research on smart sensing technology, The European Battery 2030+ roadmap funded three projects in this field – INSTABAT, SENSIBAT, and SPARTACUS projects with the goals of increasing battery safety, enhancing lifetime, improving safety, and reducing the environmental impact. The first two focus on internal sensing devices, and the last one on external sensing [21,22].

The primary goal of the INSTABAT project is to develop a proof of concept of smart sensing technology to improve Li-ion batteries' safety, performance, and lifetime. These properties are enhanced by implementing smart sensing technologies monitoring in real-time key parameters like heat flow, temperature, Li^+ concentration and distribution, impedance, and electrochemical

potential. The smart sensing technology consists of four physical sensors embedded into a cell and two virtual sensors. These sensors will provide continuous information about the key parameters, allowing us to correlate the evolution of these parameters with the physicochemical degradation. The INSTABAT project plays a crucial role in improving accuracy to enable safer cycling at extreme conditions and enhancing high-power charging for electric vehicles [5].

1.4 Li-ion Battery Anode Materials

The negative electrode acts as a host structure for Li-ions during lithiation (charging). In order to reversibly store as many Li-ions as possible, maximize energy density, and still maintain the safety of a battery, negative electrode material must meet numerous requirements [9].

To begin with, negative electrode material must be able to store as many Li-ions per mass or volume as possible and have a low (de)lithiation potential *vs.* Li^+/Li to provide high energy density. Another crucial aspect is the material's ability to maintain structural stability during cycling. Drastic, irreversible structural changes and volume expansion can lead to material degradation, irreversible consumption of active material, and, therefore, decreased battery safety and cycling lifetime. In addition to these requirements, a suitable material must possess sufficient electron conductivity, and chemical and thermal stability, not react with an electrolyte, and have a low cost [9]. Fulfilling all these requirements is difficult, and compromises must be made.

Despite not meeting all the demands for a negative electrode material, graphite is the most common and well-studied negative electrode material for LIBs. Graphite is one of the main allotropes of carbon, having a hybridization state of sp^2. Due to the sp^2 type of hybridization, carbon atoms are arranged hexagonally into atom-thick layers known as graphene. Graphene layers are stacked on each other and linked by weak van der Waals forces (Figure 2). The sequence of stacking in graphite most commonly follows a hexagonal (-ABABAB-) stacking order, with a distance of 3.35 Å between adjacent graphene layers [23,24].

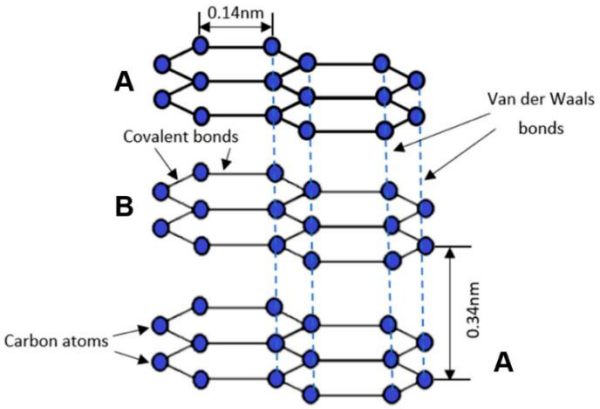

Figure 2. Graphite structure with hexagonal (-ABABAB-) stacking order [25].

Graphite has a moderate theoretical and practical specific capacity (372 mAh g^{-1} and 350 mAh g^{-1}, respectively) compared to novel negative electrode materials [26]. Alloy and conversion types of materials can have a theoretical capacity of up to 10 times higher (e.g., silicon has a theoretical capacity of 3579 mAh g^{-1}) than graphite, making them attractive alternatives [27,28]. However, novel materials, like silicon-based negative electrode materials, have demonstrated large volume expansion of up to 300% and higher Li-ion intercalation potential (E = ~0.4 V *vs.* Li^+/Li), resulting in reduced cycling life and energy density [27]. In addition to a relatively small volume expansion of 13.2% [29], compared to alloying materials, and low intercalation potential (E <0.1 V *vs.* Li^+/Li), other advantages of graphite are cost-effectiveness, high electronic conductivity, stability, and long cycling life [23]. Due to these reasons, graphite still dominates the market.

1.4.1 Lithiation and Delithiation of Graphite

The overall reaction mechanism of lithiation and delithiation of graphite can be described with Equation 1.2. However, the final intercalation compound LiC_6 is formed and decomposed back to graphite through multiple stages (Figure 3). When Li-ions intercalate into graphite, they fill interlayer spaces between graphene sheets, forming Li_xC_6 ($0 < x < 1$) intercalation compounds. This is known as a staging of graphite. The intercalation compounds are referred to as stage n (n = 1L, 4L, 3L, 2L, 2, and 1), where n corresponds to the number of graphene layers between two interlayer spaces filled with Li-ions, and L to liquid-like behaviour (disordered) in an interslab [30–32]

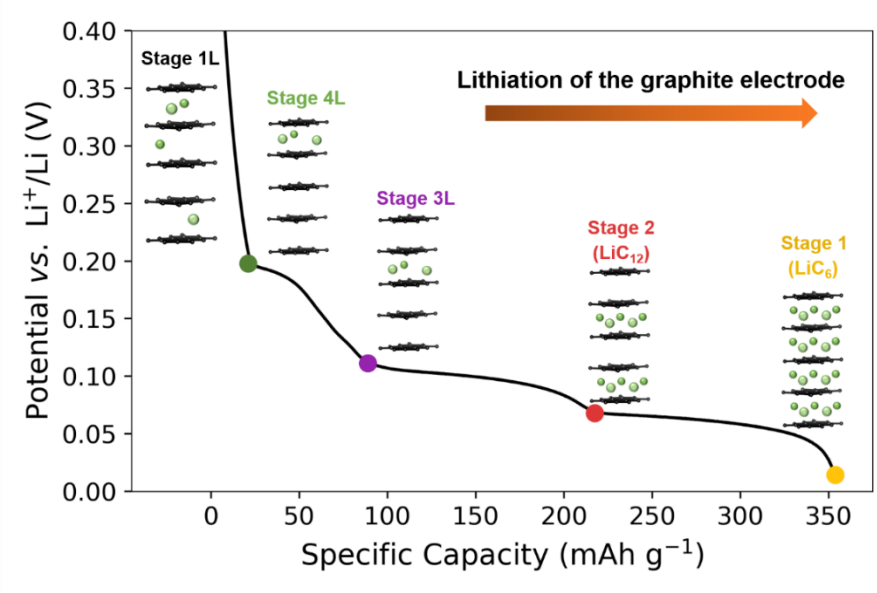

Figure 3. Simplified staging mechanism of the graphite electrode during the charging process (lithiation). Lithiation starts with the formation of stage 1L, followed by transitions to liquid-like stages of 4L and 3L, and ordered stages of 2 and 1. Lithiation ends with the formation of stage 1, also known as LiC_6.

The lithiation of graphite starts with the formation of the solid-solution phase, also known as stage 1L, in which disordered intercalation of Li-ions occurs into every interslab above potential E = 0.2 V (*vs.* Li^+/Li). While the exact number of phases and details of the transitions are still under debate, there is a consensus that the remaining Li-ions intercalation occurs through stage 1L → stage 4L → stage 3L → stage 2/2L. It has been demonstrated that in stages 4L (E = 0.11 V *vs.* Li^+/Li) and 3L (E = 0.09 V *vs.* Li^+/Li), Li-ions are randomly occupying every fourth and third interslab, respectively [31–33].

In stages 2 and 2L, every second interlayer space between graphene sheets is occupied by Li-ions. The only difference between these two stages is that in stage 2, Li-ions are arranged in order, and in stage 2L, Li-ions are disordered. During lithiation or cycling at high current rates, only stage 3L → stage 2 transition is observed, and stage 2L is skipped. It has been reported that transition from stage 3L to stage 2L is only present at extremely slow current rates, and because of kinetic limitations, it is mainly observed during delithiation (discharging) [33,34]. The lithiation ends with the formation of stage 1 (E = 0.05 V *vs.* Li+/Li), also known as LiC_6, where Li-ions occupy every interlayer space between graphene sheets [32,33].

1.5 X-Ray Diffraction (XRD)

X-ray diffraction (XRD) is a powerful technique used to characterize crystalline materials, providing information about crystal structures, phases, atomic occupation, lattice parameters, and crystal defects, among other properties [35].

The fundamental principle of XRD involves the interaction of monochromatic X-rays with a sample. In order to study crystalline materials on an atomic scale, the wavelength of X-rays must be in the same magnitude as the spacing between atoms in the sample. A monochromatic X-ray beam with a wavelength λ (nm), known as an incident X-ray beam, is directed towards the sample at an angle θ (Figure 4a). When the incident X-rays interact with the sample, they are elastically scattered by electrons within the crystal lattice. The angle between scattered and incident X-rays is referred to as a diffraction angle (2θ). If the elastically scattered X-rays satisfy Bragg's law (Figure 4a), constructive interference occurs, resulting in the appearance of a diffraction maximum (Figure 4b). By measuring the scattered intensities of these diffraction maxima and varying the diffraction angle between the incident beam and the sample, it is possible to obtain information about the crystallographic phases and properties of the sample [35,36].

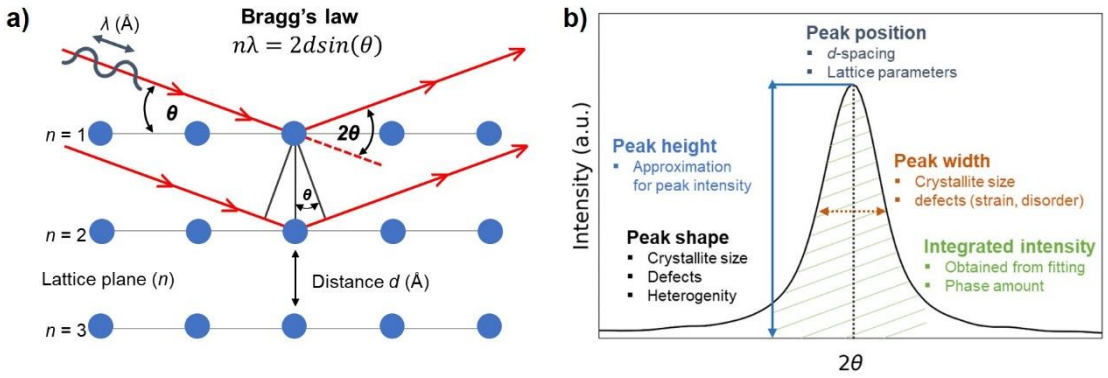

Figure 4. a) Bragg's law of diffraction, where n is the lattice plane, d is the distance between lattice planes in Å, λ is the wavelength of the incident X-rays in Å, θ, and 2θ are angles between incident X-rays and diffraction angle, respectively, **b)** Peak properties commonly used as a first approximation to evaluate diffraction patterns.

The 2θ position of a diffraction peak, i.e., constructive interference maxima, corresponds to the interplanar distance between atoms, d, also called d-spacing, from which the constructive interference maxima comes. The concentration of a phase can be determined by integrating the area under a diffraction peak – referred to as integrated intensity [37]. In order to obtain more detailed and precise information about the crystal structure of a sample, synchrotron radiation can be used instead of X-rays produced by smaller sources present in a laboratory setting.

1.6 Synchrotron Radiation

Synchrotron radiation is one of the most powerful tools to study the properties of matter. At synchrotron facilities, electrons are accelerated near the speed of light. After acceleration, electrons are directed into a synchrotron ring, where they are kept moving at relativistic speed in a circular trajectory by using a magnetic field. Due to the change in direction at relativistic speed, electrons emit electromagnetic radiation, also known as synchrotron radiation [38].

Synchrotron radiation contains high-energy X-rays, which have numerous advantages over X-ray radiation produced by laboratory sources. The most important ones for battery applications are the high brilliance and energy of emitted radiation. Brilliance refers to the intensity and coherence of the X-ray beam produced by the synchrotron source, playing a crucial role in the quality and sensitivity of an experiment. High brilliance enables the detection of weaker signals; thus, less sample is required. In addition to sensitivity, it allows for rapid data acquisition and, therefore, reduces experiment time. High energy enables a high penetration depth, which is of particular interest for measurements through battery casings. Due to all the advantages that synchrotron sources offer, they are widely used to investigate fundamental processes taking place in batteries and especially for *operando* measurements. *Operando* refers to an experiment where the diffraction patterns are collected while the battery operates in its working conditions [39,40].

Operando experiments enable to gain insight into the relationship between structural changes and electrochemical processes in batteries while they are operating in practical working conditions (charged and discharged) [40]. Many researchers have used the *operando* wide-angle X-ray scattering (WAXS) technique to understand the (de)lithiation mechanisms of different negative and positive electrode materials [41,42]. Tardif *et al.* conducted an *operando* micro-diffraction experiment where they demonstrated the evolution of the Li-ions gradient in the graphite electrode while the C-rate was increased [43]. Studying the lithiation of the graphite electrode at high C-rates is only possible due to rapid data acquisition.

WAXS experiments in synchrotron facilities can either be carried out in transmission or reflective mode. In transmission mode, the incident X-ray beam (Figure 5a) goes through the sample. As the incident X-rays interact with the sample, they scatter in various directions due to the random orientation of particles and form characteristic Debye-Scherrer diffraction rings. These rings are captured and recorded by a 2D detector. Each Debye-Scherrer ring corresponds to an exact phase with a specific scattering vector Q ($Å^{-1}$). The scattering vector Q is defined as the difference between the wave vector of the incident X-rays (k_0) and the wave vector of the scattered X-rays (k_f) (Figure 5a). The Q value obtained from the Debye-Scherrer rings can be used to identify the crystallographic phases present in the sample. By applying the relationship between the scattering vector Q (Equation 2.1) and Bragg's law (Equation 2.2), it is possible to find the d-spacing values (Equation 2.3) and to determine the crystalline lattice parameters [37,44].

$$Q = \frac{4\pi}{\lambda}\sin(\theta) \tag{2.1}$$

$$\lambda = 2dsin(\theta) \tag{2.2}$$

$$Q = \frac{2\pi}{d} \tag{2.3}$$

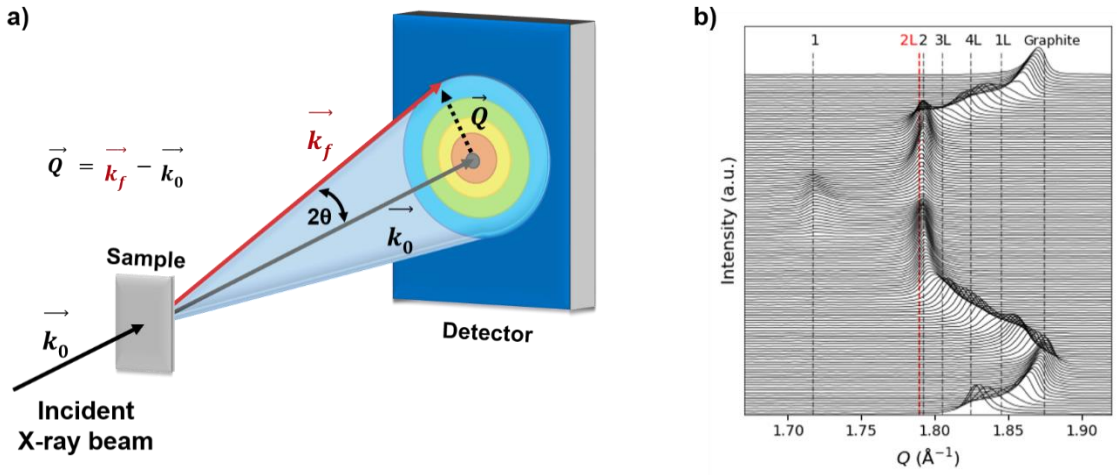

Figure 5. a) Schematic illustration of WAXS experiment in transmission mode, where k_0 is the wave vector of the incident X-rays, k_f is the wave vector of the scattered X-rays, and Q is the scattering vector. **b)** Structural evolution of the graphite electrode during (de)lithiation.

The scattering vector Q is preferred over the diffraction angle 2θ in synchrotron experiments. As explained before, the 2θ value depends on the used wavelength of radiation. For clarity, Q values are used to describe crystallographic phases because they are independent of the X-rays' wavelength. In the context of graphite, each intercalation compound formed during the lithiation of the graphite electrode has its characteristic Q values. For LiC_6 and pure graphite, corresponding 1st-order Q-values in the Q-range of 1.70–1.90 Å^{-1} are 1.70 Å^{-1} and 1.875 Å^{-1}, respectively (Figure 5b) [31].

1.7 The Aim of The Thesis

The data analysed in this thesis was collected during the *operando* wide-angle X-ray scattering experiments conducted as a part of the INSTABAT and BIGMAP projects. The goal of the INSTABAT project is to provide a proof of concept of smart sensing technologies and functionalities. By integrating smart sensing technologies into a battery cell, they aim to develop a battery cell capable of monitoring key parameters in *operando*, correlate the evolution of key parameters with the physicochemical degradation, and improve battery performance and safety.

This thesis aims to contribute to the goals of the INSTABAT project by providing insight into structural changes in a commercial multi-layered electrode prismatic pouch cell equipped with a reference electrode and temperature-sensitive optical fiber at various C(D)-rates. The first part of the thesis aims to validate the structural changes occurring in the graphite electrode of a single-graphite electrode layer cell (hereafter referred to as the single-layer cell). The analysed data is used as a reference point to understand the (de)lithiation mechanism and kinetics of the graphite electrode in the multi-layered cell.

The second part of the thesis focuses on investigating the structural changes occurring within the graphite electrode near the optical fiber inserted into the multi-layered cell, as well as in the middle of the multi-layered cell. By analysing the diffraction patterns obtained near the optical fiber, the study aims to provide insight into how the presence of the optical fiber affects the cell's geometry and graphite lithiation. Furthermore, the study seeks to determine whether the data collected near the optical fiber accurately represents the entire cell or only a localized area. The latter is crucial to estimate the heterogeneities in the state of charge occurring within a battery cell.

In conclusion, this work intends to provide answers to several important questions:

1. What is the impact of the configuration and geometry of a multi-layered cell on the lithiation kinetics within the graphite electrode?
2. Does the insertion of an optical fiber into a commercial multi-layered prismatic pouch cell disrupt the lithiation kinetics of the graphite electrode near the optical fiber?
3. What is the impact of varying C-rates on the lithiation kinetics, specifically in terms of differences between the optical fiber position and the central area of the multi-layered cell?
4. Does the data obtained near the optical fiber accurately represent the entire cell, or does it exclusively describe the characteristics of the region around the optical fiber?

By addressing these inquiries, the study aligns directly with the goals of the INSTABAT project, contributing to the development of batteries capable of providing accurate information on key parameters in *operando*. The study provides valuable insights into both structural changes within the graphite electrode and the impact of the optical fiber integrated into the multi-layered cell. These insights are crucial for optimizing high-power charging and cycling of batteries at extreme conditions, especially in the context of electric vehicle applications.

2. Experimental Methods

The *operando* wide-angle X-ray scattering experiment was carried out at European Synchrotron Research Facility in February 2022 by Oliver Raccurt (LITEN, CEA), Sylvie Genies (LITEN, CEA), Cédric Septet (LITEN, CEA), Romain Franchi (LITEN, CEA), Sandrine Lyonnard (IRIG, CEA), Samuel Tardif (IRIG, CEA), and Claire Villevielle (LEPMI).

2.1 Electrochemical Cells and Their Properties

Two lithium-ion battery cells were studied in the *operando* wide-angle X-ray scattering experiment – single-layer and multi-layered cells. Both cells consisted of $LiNi_{0.6}Mn_{0.2}Co_{0.2}O_2$ (NMC622) positive electrode and commercial graphite negative electrode. The multi-layered cell, with a practical capacity of 1.1 Ah, and single-layer cell electrode materials were provided by Li-Fun Technology (Shuzhou, Hunan, China). The electrolyte used for both cells was 1 M $LiPF_6$ in a mixture of ethylene carbonate (EC) and ethyl methyl carbonate (EMC) (3:7 in volume ratio) with 2 mass% of vinylene carbonate (VC) additive. Detailed information about both the single-layer and the multi-layered cell electrodes and their properties are provided in Appendix A1, Appendix A2, and Appendix A3.

The single-layer cell with a practical capacity of 25.6 mAh was assembled by the research group at LITEN (CEA). The single-layer cell consisted of one positive electrode (NMC622) and one negative electrode (graphite) separated by an Al_2O_3/polyethylene composite separator. The current collectors of the negative (Cu) and positive electrodes (Al) were coated on one side and had a geometrical area of 12.25 cm^2 and 10.24 cm^2, respectively (Appendix A1).

The multi-layered pouch cell with prismatic jelly roll configuration was obtained from Li-Fun Technology in a dry state (without the electrolyte). The positive (NMC622) and the negative electrode (graphite) had a double-side coating, meaning both sides of a current collector were coated with the electrode material (Appendix B1). The total coating area for the negative and the positive electrodes was 461.4 cm^2 and 436.74 cm^2, respectively, with the negative electrode being in excess. The multi-layered cell was disassembled in an argon-filled glovebox where the electrolyte, a reference electrode, and a temperature-sensitive sensor (optical fiber) were added into the cell (Appendix B2b). Subsequently, the electrodes separated with the polyethylene separator were wound back into a prismatic jelly roll configuration, with a total of 27 layers, comprising seven layers of the negative electrode, five layers of the positive electrode, and 15 layers of the separator. Finally, the multi-layered cell was vacuum-sealed to ensure a hermetic and stable enclosure for further examination.

2.1.1 Reference Electrode and Optical Fiber Sensor

The multi-layered cell was equipped with two sensors – a reference electrode and a temperature-sensitive optical fiber. LFP ($Li_{(1-x)}FePO_4/LiFeO_4$, E = 3.424 V *vs.* Li^+/Li) coated Au reference electrode sensor with antenna design (Appendix B3a) was integrated into the multi-layered cell to obtain information about absolute potential, impedance, and polarization.

The thermoluminescent optical fiber coated with GdV_2O_4 particles doped with Er^{3+} and Yb^{3+} (diameter = ~280 µm) was used to monitor the internal temperature by measuring luminescence intensity (Appendix B3b). The sensor was positioned at the center of the multi-layered cell between two separators in the z-direction.

In addition to the sensors integrated into the multi-layered cell, seven thermocouple sensors were placed on the outer side of the cell. The exact positions of the thermocouple sensors are shown in Appendix B4b.

2.2 Wide-Angle X-Ray Scattering Experiment

The *operando* wide-angle X-ray scattering (WAXS) experiment was conducted at European Synchrotron Radiation Facility (ESRF, Grenoble, France) on the beamline BM02 in February 2022. The energy of the incident X-ray beam was fixed at 25 keV (λ = 0.4959 Å) and size at 60x60 µm. 2D-diffraction patterns were collected in transmission mode, allowing X-rays to pass through the samples, and recorded using an imXPAD WOS detector. The Q-scale calibration was performed using chromium oxide (Cr_2O_3) and lanthanum hexaboride (LaB_6) as reference materials. The distance between the detector and the sample was estimated to be 409 mm. 1D WAXS diffraction patterns were obtained by azimuthal integration of the recorded 2D patterns using the PyFAI library.

The WAXS experiments of the single-layer and the multi-layered cells were carried out in *operando* mode, meaning the data were collected while charging and discharging the cells. All the current rates used to charge and discharge both cells are shown in Appendix C1. The hold step at U = 4.2 V was applied after each charge step to stabilize the system and ensure the maximum state of charge. After every discharge step, a standby step was added to stabilize the cell's voltage.

2.2.1 Cells Designs for The Operando WAXS Experiment

Both cells were placed between metal plates. In order to allow the X-ray beam to pass through the cell without interference from the sample holder, strategically positioned holes were drilled into metal plates. For the single-layer cell measurement, a single hole with a diameter of 1 mm

was drilled through the metal plates at the center of the cell. For the multi-layered cell, three holes with a diameter of 1 mm were drilled near the reference electrode, near the optical fiber, and the center of the cell Figure 6b and 6d. The hole at the center of the cell was used to collect diffraction patterns from the mechanically undisrupted area.

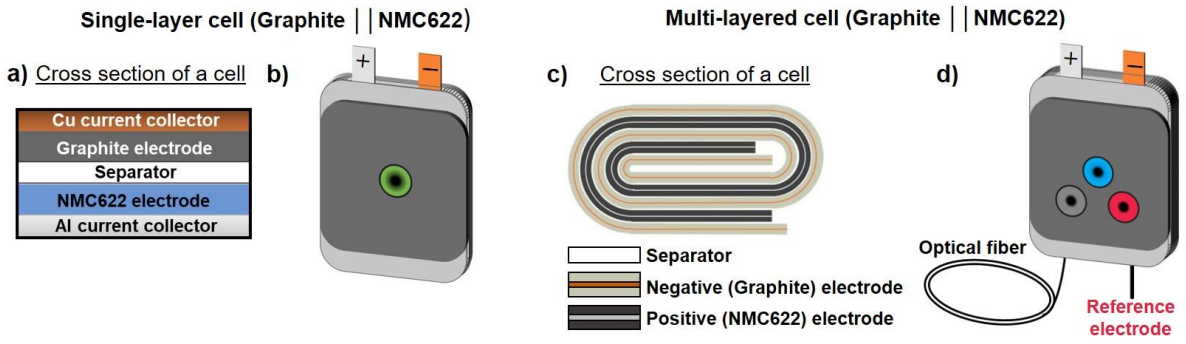

Figure 6. a) Illustrative stacking order, and **b)** configuration of the single-layer cell for the WAXS experiment. **c)** Illustrative jelly-roll configuration [45], and **d)** location of the drilled holes of the multi-layered cell for the WAXS experiment.

2.2.2 Collecting Diffraction Patterns from Different Positions

The measurement of both cells started with collecting diffraction patterns from nine different locations within a hole (referred to as MESH measurement) while cycling cells at slow C-rates. The aim of the MESH measurement was to understand if the lithiation of the graphite electrode is homogeneous over the entire electrode. The scanning order of the points was 3→2→1→6→5→4→9→8→7 and the counting time (ct) per point was 30 seconds (Figure 7a). C(D)-rates used during the MESH measurement for the single-layer and the multi-layered cells are shown in Appendix C1. Positions of each scanning point of the single-layer and the multi-layered cells are provided in Appendix D1 and Appendix D2.

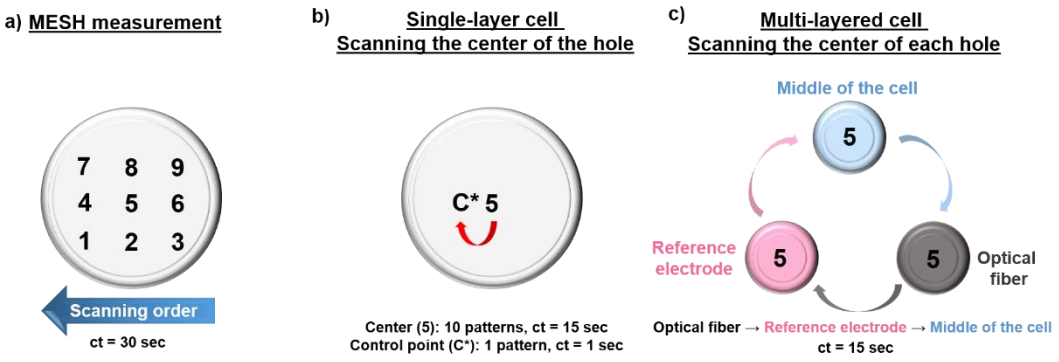

Figure 7. Scanning order of **a)** beginning of measurements with the MESH, **b)** measuring the center of a hole in the single-layer cell after the MESH measurement continuously, and **c)** measuring the center of each hole in the multi-layered cell.

After the single-layer cell MESH measurement, the center of a hole was continuously scanned to record structural changes at high C(D)-rates (Figure 7b and Appendix C1a). For every 10 recorded diffraction patterns (ct = 15 seconds), one was measured at a control point (ct = 1 second) to observe the effect of a long-term exposure time to the synchrotron beam.

After charging the multi-layered cell at C/2 during the MESH measurement, the multi-layered cell was rapidly discharged at 4D. During rapid discharge, diffraction patterns were collected from the center of each hole following the optical fiber → the reference electrode → the center of the cell sequence (Figure 7c). After discharging at 4D, residual discharging was performed to ensure that a fully delithiated state was achieved at the end of discharging. The discharging process was followed by charging at 2C in the same scanning sequence.

2.3 Data Analysis of The Single-Layer and The Multi-layered Cells

The data acquired from the measurements was analysed using the programming language Python on the Anaconda platform. Before the analysis, the collected data was processed in a series of steps. Baseline removal was performed using the asymmetrical least squares function. After baseline removal, the *Q*-range of each diffraction pattern was calibrated by aligning the experimental position of the Cu(200) peak with its corresponding theoretical value of 3.4756 Å^{-1}. Finally, peaks originating from the cell casing, present in the diffraction patterns, were removed. Since the position (Q_{values}, Equation 3.1) of these peaks remained strictly identical during the measurement, it was possible to remove them by applying the equations system shown below (Equations 3.1–3.4). Firstly, the minimum intensity value was found at every given *Q*-value over the data set (Equation 3.3). Minimum intensity values were found for every scanning position in the single-layer and the multi-layered cell (Equation 3.2). After obtaining a data set consisting of only minimum intensity values at every *Q*-value, they were subtracted from the original intensities (Equation 3.4).

$$Q_{values} = \{Q_0, Q_1, \dots, Q_k\} \tag{3.1}$$

$$Original\ dataset = \begin{Bmatrix} Data_0| & I_0Q_0 & I_{0+1}Q_1 & \dots & I_{0+k}Q_k \\ Data_1| & I_1Q_0 & I_{1+1}Q_1 & \dots & I_{1+k}Q_k \\ \vdots & \vdots & \vdots & \dots & \vdots \\ Data_n| & I_nQ_0 & I_{n+1}Q_1 & \dots & I_{n+k}Q_k \end{Bmatrix} \tag{3.2}$$

$$I_{min} = min\big(I(Q)\big), \qquad where\ Q = Q_{0,1,\dots,k} \tag{3.3}$$

$$New\ dataset = \begin{Bmatrix} Data_0| & I_0Q_0 - I_{min}Q_0 & I_{0+1}Q_1 - I_{min}Q_1 & \cdots & I_{0+k}Q_k - I_{min}Q_k \\ Data_1| & I_1Q_0 - I_{min}Q_0 & I_{1+1}Q_1 - I_{min}Q_1 & \cdots & I_{1+k}Q_k - I_{min}Q_k \\ \vdots & \vdots & \vdots & \cdots & \vdots \\ Data_n| & I_nQ_0 - I_{min}Q_0 & I_{n+1}Q_1 - I_{min}Q_1 & \cdots & I_{n+k}Q_k - I_{min}Q_k \end{Bmatrix} \quad (3.4)$$

In this work, only diffraction patterns from the single-layer cell measurement were suitable for fitting. Indeed, the multi-layer cell peaks have complex shapes due to the superposition of patterns originating from the different layers. The Pseudo-Voigt function (0.5 Lorentz function and 0.5 Gaussian function) was used to fit the data obtained from the *operando* WAXS experiment. Overall, five distinct peaks corresponding to Li_xC_6 phases were observed in the first-order graphite region *Q*-range (1.70–1.90 $Å^{-1}$). Hence, during the graphite (de)lithiation stages 1L, 4L, 3L, 2+2L, and 1, with peak bounds of 1.875–1.845 $Å^{-1}$, 1.840–1.825 $Å^{-1}$, 1.820–1.810 $Å^{-1}$, 1.799–1.777 $Å^{-1}$, and 1.725–1.705 $Å^{-1}$, respectively, were considered. Phase fractions for each stage were calculated using integrated intensities obtained from fitting (Equation 4).

$$Phase\ fraction\ of\ a\ stage = \frac{Integrated\ intensity\ of\ a\ stage}{\sum_{1L+Gr,4L,3L,2+2L,1} Integrated\ intensities} \quad (4)$$

Equation 5 was applied to determine the visible peak positions in the first-order graphite region *Q*-range ($Q \in$ 1.70–1.90 $Å^{-1}$) in every diffraction pattern obtained from the multi-layered cell measurement.

$$Center\ of\ mass = \frac{Q_{peak} * Intensity_{peak}}{\sum_{Q_{values}} Intensity_{values}} \quad (5)$$

In order to estimate beam damage on the graphite electrode, a Python code developed by Thibaut Jousseaume and Samuel Tardif was used to calculate radiation dose and estimate beam damage on the graphite electrode – the code is available in GitHub repository: https://github.com/STardif/ dose_estimation. By giving information regarding the cell's components (such as the number and order of electrodes and separators), electrode materials (material, thickness, porosity, etc.), and X-ray beam (size, flux, energy, exposure time), it is possible to estimate the radiation dose and dose rate acquired by each component.

3. Results and Discussion

3.1 Electrochemistry Results

The multi-layered and single-layer cells were designed to have nominal capacities of 1.1 Ah and 25.6 mAh, respectively. Voltage (V) *vs.* Time (h) curves with applied charge and discharge rates of both cells are shown in Appendix C1. The hold step at $U = 4.2$ V was applied after each charging step to stabilize the system and ensure the maximum state of charge.

In the first cycle, the single-layer cell demonstrated a charge capacity of 25 mAh, which was 98% of the nominal capacity (25.6 mAh) (Figure 8a) at the end of the hold step. However, during cycling, the cell's capacity decreased within every cycle. By the last cycle (cycle no. 6), the charge capacity value at the end of the hold step had dropped to 92.5% of the nominal capacity. Compared to the single-layer cell, the multi-layered cell exhibited better stability, and only slight variations in charge capacity values were observed (Figure 8b). While cycling in the voltage range of 2.8–4.2 V (the first six cycles), the cell's charge capacity was between 90–92 % of the nominal capacity (1.1 Ah). In the 9th cycle, the multi-layered cell demonstrated a higher charge capacity than the previous cycles due to a wider applied voltage range of 2.8–4.35 V.

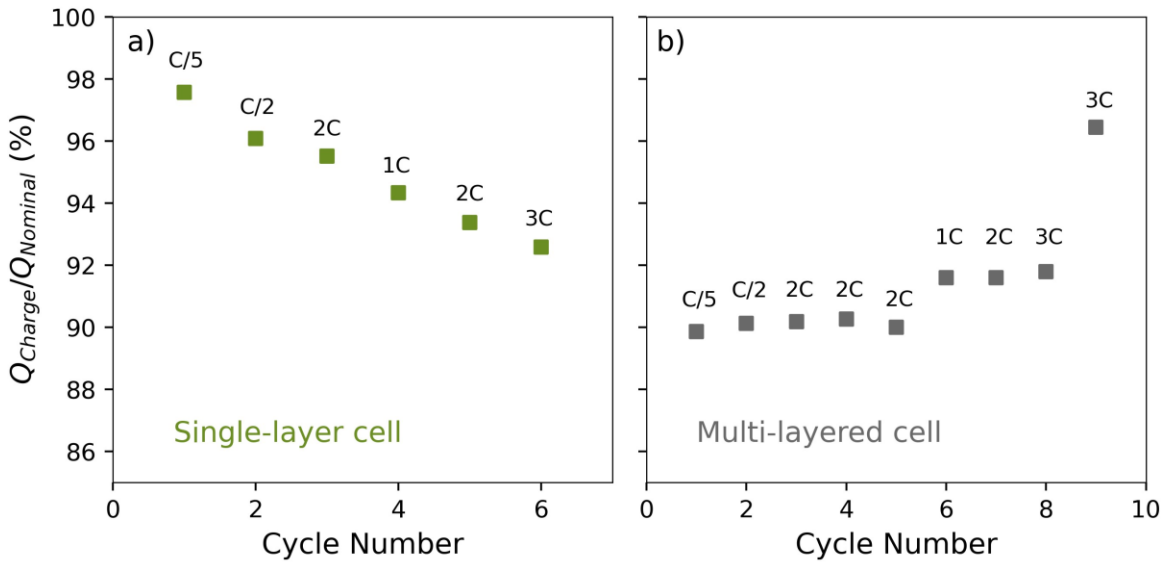

Figure 8. The ratio of measured charge capacity (Q_{Charge}) and nominal capacity ($Q_{Nominal}$) of **a)** the single-layer cell and **b)** the multi-layered cell. For the single-layer cell, the nominal capacity was 25.6 mAh, and for the multi-layered cell 1.1 Ah.

In conclusion, based on electrochemistry results, the integration of the optical fiber inside the multi-layered cell had no impact on the electrochemical performance. However, in the case of the single-layer cell, the charge capacity decreased within every cycle. The decreased capacity

can be caused by the degradation of electrode materials or electrolyte of the single-layer cell since the capacity continued dropping even if the C-rate was decreased after the third cycle.

3.2 WAXS Analysis of The Single-Layer Cell

3.2.1 The MESH Measurement of The Single-Layer Cell

The aim of the MESH measurement was to understand if the lithiation of graphite is homogeneous over the entire electrode. During the MESH measurement, diffraction patterns were collected at nine different scanning points. The scanning order over the points is shown in Figure 7a. Diffraction patterns were collected *operando* while the single-layer cell was being cycled. The MESH measurement started with residual discharging at C/5 (0–1.7 hours), followed by charging at C/5, holding a voltage of 4.2 V for 0.2 h, and discharging at C/5 up to 3.4 V (Figure 9a).

Figure 9b is a 2D plot of diffraction patterns collected in the middle of a hole (scanning point no. 5). A 2D plot is a way to present phase transitions in time; the warmer the color, the higher the intensity of a certain phase compared to others. Averaged phase fractions at different scanning points in time are shown in Figure 9c, where phase fractions show the ratios of different graphite stages present at all experimental times. The equation for obtaining phase fractions is shown in Equation 3. Error bars demonstrate the maximum and minimum phase fraction values between scanning points.

At the end of the residual discharging, the graphite electrode was in stage 1L+Gr, representing both pure graphite and the disorganized graphite structure at low Li-ion concentration intercalated in the graphite electrode. As soon as a positive current was applied, stage 4L began to form, and stage 1L+Gr disappeared totally at U = 3.55 V. Almost immediately after the disappearance of stage 1L, a continuous transition from stage 4L to 3L started taking place. The continuous transition is evident in the Q range of 1.84–1.805 $Å^{-1}$ between 2.7 to 3.5 hours (Figure 9b).

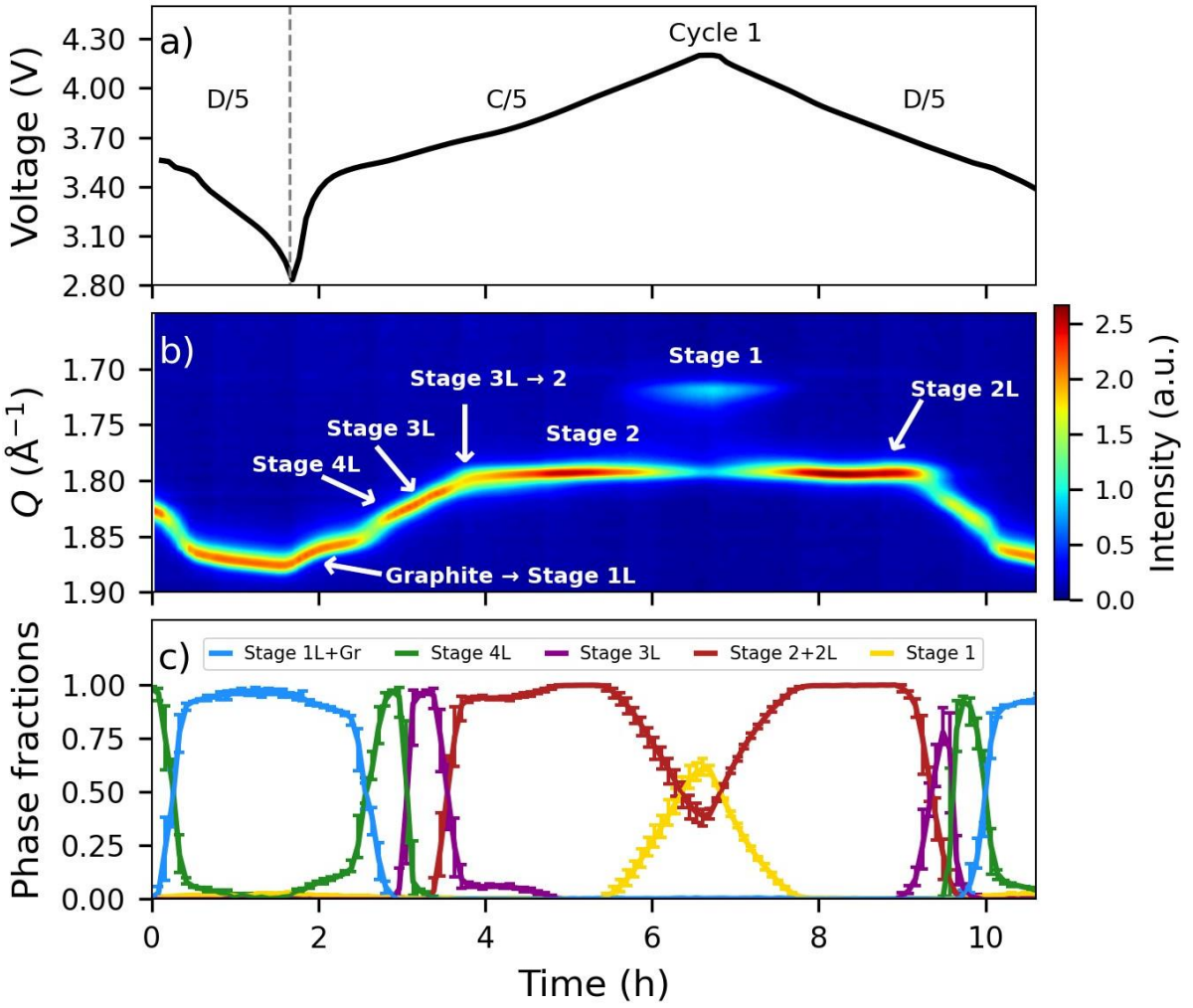

Figure 9. a) Voltage (V) change in time (h) during the MESH measurement, **b)** 2D plot (Q (Å^{-1}) *vs.* Time (h)) of scanning point no. 5 (scanning point in the middle of a cell), **c)** averaged phase fraction changes in time.

The transition from stage 3L to stage 2 is illustrated by a slope and a plateau in Figure 9c and occurred over a wide voltage range (U = 3.61–3.83 V, t = 3.3–4.8 h) compared to the previous transition. These two regions indicate that the transition occurred at two different rates. Initially, the phase fraction of stage 3L continuously decreased while stage 2 formed. Above U = 3.63 V, the transition rate slows drastically, resulting in the coexistence of stages 3L and 2. In liquid-like stages, Li-ions randomly fill the interlayer spaces of graphite. It is speculated that the transition from liquid-like stage 3L to ordered stage 2 (LiC_x, x = 12) involves the complete filling and emptying of some interlayer spaces [33], resulting in kinetic limitations and, therefore, leading to the coexistence of these two phases.

The final transition from stage 2 to 1 (LiC_x, x = 6) is the most well-understood. During this transition, every interlayer space is filled with Li-ions. At the end of the hold step, after charging at C/5 (U = 4.2 V), the phase fraction values of stage 1 and stage 2 were 0.615 (±0.03)

and 0.385 (±0.03), respectively (Figure 9c). The presence of stage 2 at the end of the hold step is a result of the designed excess capacity in the negative electrode.

At the onset of delithiation, stage 1 gradually disappeared. Once stage 1 was fully transformed into stage 2, no further changes were observed between 8–9 hours in the phase fractions. However, upon closer examination, a slight decrease in *Q* range values was noticed before the formation of stage 3L (Figure 9b). This decrease in *Q* value suggests the presence of stage 2L. The formation of stage 2L is kinetically slow and rarely observed during the lithiation process, as it involves complex structural reordering between ordered and liquid-like stages. In contrast, during delithiation, the transition from stage 2 to 2L requires less structural reorganization [33,34,46], favoring the formation of stage 2L.

In conclusion, the lithiation and delithiation processes of the graphite electrode in the single-layer cell at a slow C(D)-rate exhibit several key observations. Firstly, the lithiation process follows a sequential transition from stage 1L to stage 1, and stage 2L was detected during the delithiation process, which is in good agreement with previous studies [31,33,34,47]. Lastly, the (de)lithiation of graphite was found to be homogeneous across different scanning points, with minor variations in phase fractions.

3.2.2 The Continuous Measurement of The Center of a Hole

In order to record structural changes of graphite at high C(D)-rates, the center of a hole was continuously scanned. For every 10 recorded diffraction patterns (counting time (ct) per diffraction pattern was 15 sec), one diffraction pattern was measured at a control point (ct = 1 sec) to observe the effect of a long-term exposure time to the synchrotron beam (Appendix E ***1***).

At first glance, stage transitions while charging at C/2 (2^{nd} cycle) were comparable to C/5. However, small differences were observed. The transition between stages 3L and 2L is illustrated by two different slopes in Appendix E2a (capacity = 7–21 mAh). The transition from stage 3L to 2 was initially similar to the one observed during the MESH measurement. Nonetheless, the latter part of the stage 3L→2 transition was notably slower, resulting in a smaller amount of formed stage 1 at the end of lithiation and suggesting increased energy barriers and kinetic limitations during the lithiation [46]. The limitations in kinetics became more pronounced within every cycle. In the 6^{th} cycle, after charging at 3C, stages 1L, 3L, 4L, and 2 were present, with graphite mainly in stage 4L (Appendix E2e) at the end of the hold step. This behaviour deviates from the previous research finding in this field [34,47,48].

In order to gain further insight into this unusual behaviour, diffraction patterns from the control point were analysed. Despite poorer statistics in the collected data compared to the continuously scanned point at the center of the hole, clear contrasts in phase fractions were observed. The control point exhibited more homogeneous stage transitions (Appendix E3), and the coexistence of different stages while (de)lithiating at higher C(D)-rates aligns well with the results reported in this field [47]. The significant differences in lithiation mechanisms between the two scanned points suggest that long-term exposure to a synchrotron X-ray beam leads to irreversible changes in the graphite electrode.

3.2.3 Beam Damage on The Graphite Electrode

Beam damage occurs over time when an area of the material is irritated with a high-energy synchrotron beam. A high-energy synchrotron beam can interact with the electrode surface, leading to altered surface chemistry, irreversible electrode changes, and degradation of various electrochemical cell components [49]. While the effect of beam damage on electrode materials, particularly graphite, is not yet fully understood, it has been observed that phase transitions can be delayed in areas where beam damage occurs. In the case of graphite electrodes, the organic components, especially the binder, are believed to be the most susceptible to beam damage [50]. High doses of radiation can cause polymer binder to degrade, leading to decreased contact between the current collector and carbon particles.

In order to analyse data from the multi-layered cell, it is crucial to consider the occurrence of beam damage. It has been reported that the microstructure of a graphite electrode undergoes modification at radiation doses between 1–4 MGy, and (de)lithiation kinetics are significantly affected beyond 11 MGy [51]. Considering both calculations and the findings discussed earlier, a radiation dose threshold of 1.75 MGy was established as the upper limit for data without beam damage (Appendix E4). Understanding when beam damage occurs on an electrode is vital for accurately analysing and interpreting collected data.

3.3 WAXS Analysis of The Multi-Layered Cell

The geometry of the multi-layered cell and the locations of the holes (near the reference electrode, the optical fiber, and at the center of the cell) are shown in Appendix B2 and Appendix B4a. Only the data collected during residual discharging, MESH measurement, discharging at 4D+D/5, and charging at 2C were analysed. The rest was influenced by beam damage (Appendix E4a).

3.3.1 Lithiation Mechanism of The Single-Layer Cell vs. The Multi-Layered Cell

Structural changes of the single-layer and multi-layered cells were compared to understand how multi-layered cell geometry affects graphite (de)lithiation mechanism and kinetics. To gain insight into the impact of the geometry, the data from the hole in the middle of the multi-layered cell was used for comparison.

At the beginning of charging at C/5, the cells were in a fully delithiated state. The multi-layered cell demonstrated a slightly wider graphite peak than the single-layer cell (Figure 10a). The variation in peak widths is caused by the multi-layered cell geometry. In the multi-layered cell, there are several layers of the graphite electrode. Each graphite electrode layer has a slightly different distance to the detector, hence slightly different *Q*-values for the graphite peak. These peaks are close and convolute into a single Gaussian peak with a larger width than the graphite peak from the single-layer cell.

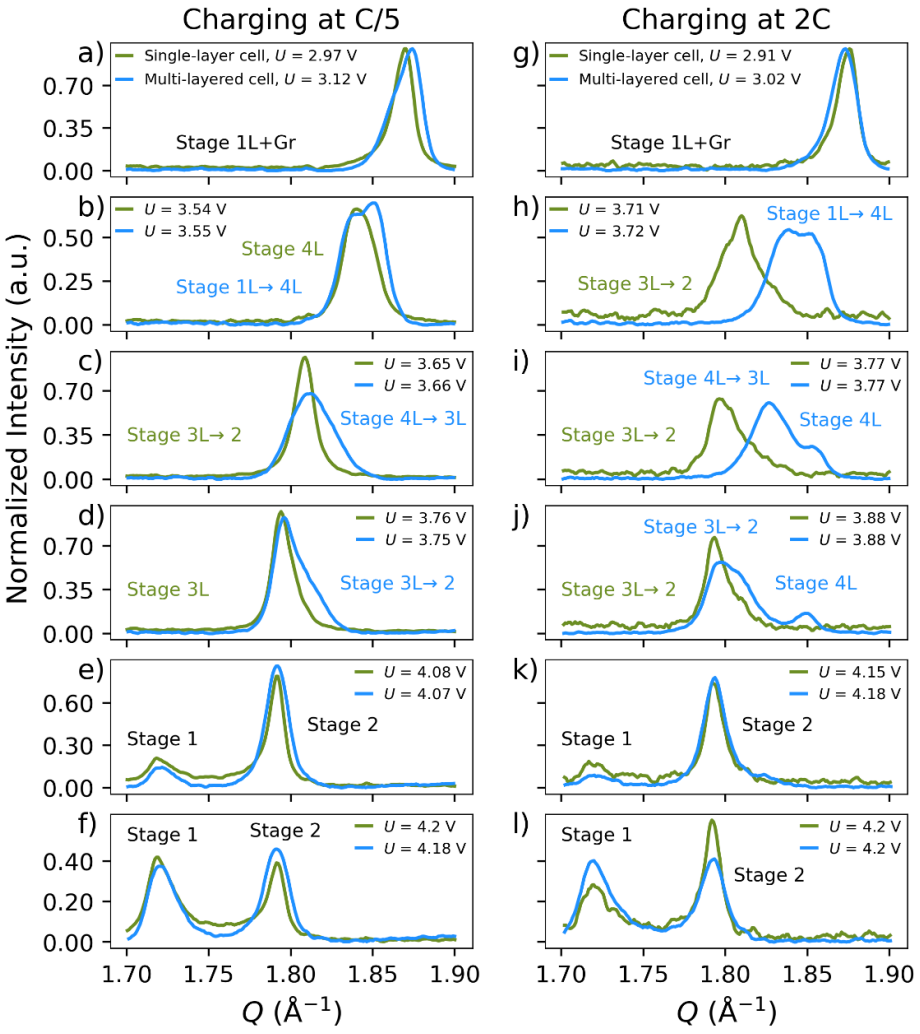

Figure 10. Diffraction patterns were collected from the single-layer cell and the multi-layered cell during charging **a-f)** at C/5 and **g-l)** 2C. The single-layer cell diffraction patterns shown in figures g–l were measured at the control point.

At the voltage of $U = 3.54$ V, the single-layer cell was in stage 4L (Q = ~1.840 Å^{-1}) (Figure 10b). However, at the same voltage, the multi-layered cell exhibited a transition from stage 1L (Q = ~1.855 Å^{-1}) to 4L (Figure 10b). Similar observations were made during the stage transitions from stage 4L to 3L and stage 3L to 2 (Figure 10c-e). Nonetheless, at the end of the hold step ($U = 4.2$ V), the peak profiles of stage 1 and stage 2 were comparable between the single-layer and the multi-layered cells (Figure 10f). This indicates that 1) polarisation in the multi-layered cell is higher, leading to a lower state of charge for a given voltage compared to the single-layer cell, and 2) the lithiation process is more heterogeneous in the multi-layered cell, and heterogeneity is probably due to difference in the state of charge in between graphite layers.

The observed lagged stage transitions of the multi-layered cell can be attributed to the specific flat jelly roll geometry of the multi-layered cell (Appendix B1). In this geometry, some of the outer regions of the double-side coated graphite electrode are not directly facing the positive electrode but rather the cell's casing. However, despite this configuration, no graphite peaks were detected at the end of the lithiation process, indicating that these outer regions were also lithiated. Bond *et al.* demonstrated through micron-scale X-ray computed tomography that in Li-FUN type of cells, the electrolyte also wets the outer regions of the graphite electrode [52]. The electrolyte, serving as a conductive medium, facilitates Li-ions' transport. Due to the design of the multi-layered cell, the migration of Li-ions towards the outer regions of the graphite electrode occurs through the bulk of the jelly roll, leading to an extended diffusion time for Li-ions and consequent delays in the lithiation process [53]. The delayed lithiation of the outer regions of the graphite electrode was further confirmed by a post-mortem analysis of a cylindrical cell conducted by Wilhelm *et al.* [54]. Collectively, these findings indicate that the lags in stage transitions were mainly caused by the slower lithiation kinetics of the outer regions that are not directly facing the positive electrode.

Both cells demonstrated broader peaks at higher C-rates compared to lower C-rates (Figure 10g-l). Moreover, a shoulder peak at higher Q-values was observed in the multi-layered cell at $U = 3.77$ V and $U = 3.88$ V (Figure 10i-j). Regarding the broader peaks for both cells, Tardif *et al.* showed that Li-ions distribution in the graphite electrode becomes more heterogeneous at higher C-rates. Specifically, the top part of the graphite electrode exhibits a higher lithiation degree compared to the bottom part, which is closer to the current collector [43]. This type of depth-depending heterogeneity is present in both cells and can explain part of the broadening observed. The presence of the shoulder peak exclusively in the multi-layered

cell suggests that delayed lithiation of the outer regions becomes more prominent at higher C-rates (Figure 10g-l). Therefore, to comprehend the structural changes occurring near the reference electrode and the optical fiber in the multi-layered cell, it is essential to consider both delayed lithiation of the outer regions of the graphite electrode and the heterogeneous distribution of Li-ions within the graphite electrode at higher C-rates.

3.3.2 The Impact of The Optical Fiber on Graphite Lithiation at Various C-Rates

By understanding the influence of both the C-rate and the geometry of the multi-layered cell, it is now possible to analyse the structural changes and kinetics near the optical fiber. It is important to note that the behaviour described in the previous chapter was considered as normal behaviour for the multi-layered cell.

3.3.2.1 Observations While Charging at C/5 and 2C

At the beginning of charging at C/5, the profile of the graphite peak was nearly identical between diffraction patterns collected near the reference electrode, near the optical fiber, and in the middle of the cell (Appendix F1a). However, some differences were observed. First, comparing the center and the reference electrode position, a small peak at Q = 1.805 $Å^{-1}$ was observed in the delithiated state, which is most likely coming from LFP (the reference electrode material) (Appendix F1a) [55]. Moreover, during the lithiation, small differences in peak shapes between the reference electrode and the center of the cell positions were observed and attributed to a 4.5 min time interval between these two measurements (corresponding to 1.5% state of charge difference) (Appendix F1a-f). Overall, the reference electrode appeared to have nearly no effect on the (de)lithiation kinetics.

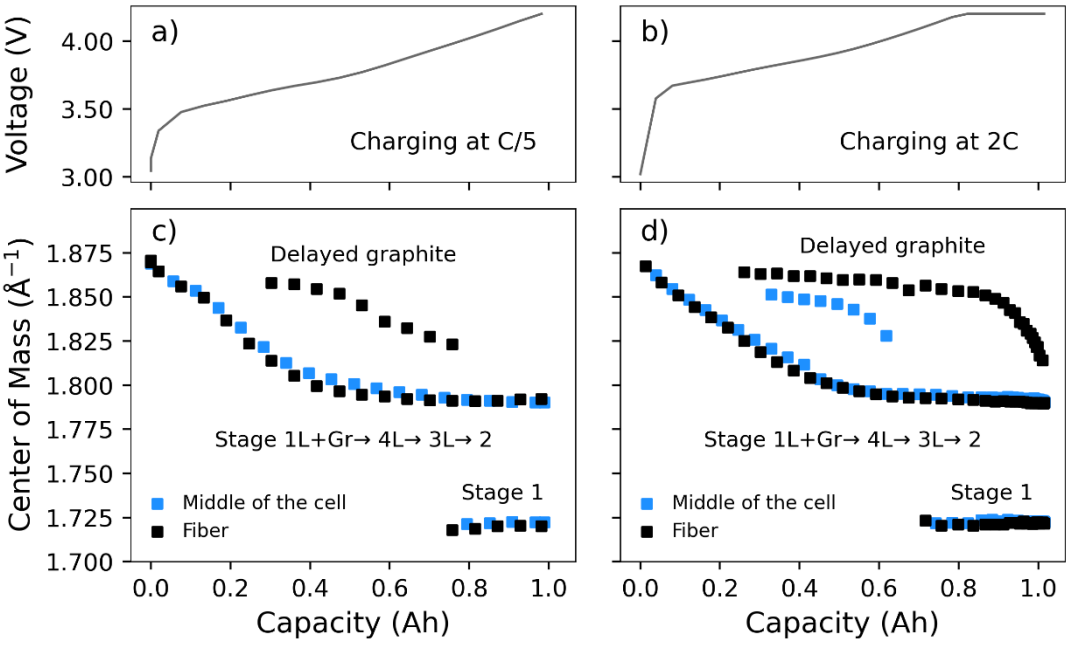

Figure 11. Voltage (V) *vs.* Capacity (mAh) while charging at **a)** C/5 and **b)** 2C. Center of Mass (Å^{-1}) evolution while charging at **c)** C/5; and **d)** 2C.

Furthermore, when comparing diffractograms from the center and the fiber positions at U = 3.64 V during the 4L → 3L transition, a small additional peak at Q = ~1.86 Å^{-1} was observed in the optical fiber pattern (marked ♦ in Appendix F1). The well-separated peak indicates delayed graphite lithiation in some regions around the optical fiber. The distinct separation was observed all along the charging, indicating a severe delay in graphite lithiation around the optical fiber (Figure 11c). Nevertheless, the state of charge finally equilibrated during the hold step at U = 4.2 V, and no significant differences in the state of charge were observed between areas near the optical fiber and in the middle of the cell (Figure 11c, Appendix F1f). It can be concluded that at a slow C-rate, the optical fiber slightly disrupts the lithiation, but the overall lithiation mechanism remains largely consistent with normal behaviour.

The presence of a delayed phase of graphite became more prominent when the multi-layered cell was charged at a higher C-rate of 2C and remained present until the end of the hold step at U = 4.2 V (Figure 11d, Appendix F1*l*). It is fair to assume that the insertion of an optical fiber might have deformed the electrode layers and possibly increased the distance between electrodes around the optical fiber, resulting in kinetic limitations. Furthermore, the distinct separation of peaks between the delayed and normal graphite regions near the optical fiber

suggests considerable differences in the state of charge between the areas around the optical fiber and the center of the cell throughout charging.

3.3.2.2 Observations While Discharging at 4D

At the beginning of the fast discharging at 4D, stages 1 and 2 were present near the optical fiber, the reference electrode, and the middle of the cell (Figure 12a-c). Around the optical fiber, delayed graphite was observed at Q = 1.83 Å^{-1}. As soon as the high negative current was applied, stage 1 started to disappear. All positions demonstrated stage transition in the sequence of stage 2→stage 3L→stage 4L→stage 1L. At the end of the fast discharging, mainly stages 2 and 1L, along with a small amount of stage 4L, were present (Figure 12b). The presence of stage 2 can be attributed to kinetic limitations [33,34,46]. A higher amount of 3L/4L was present near the optical fiber compared to the center of the cell. This can be attributed to delayed (de)lithiation of some regions near the optical fiber. After discharging at 4D, the multi-layered cell was fully discharged at D/5 (Figure 12d), and all position patterns featured a single peak corresponding to graphite at the end of this residual slow discharge.

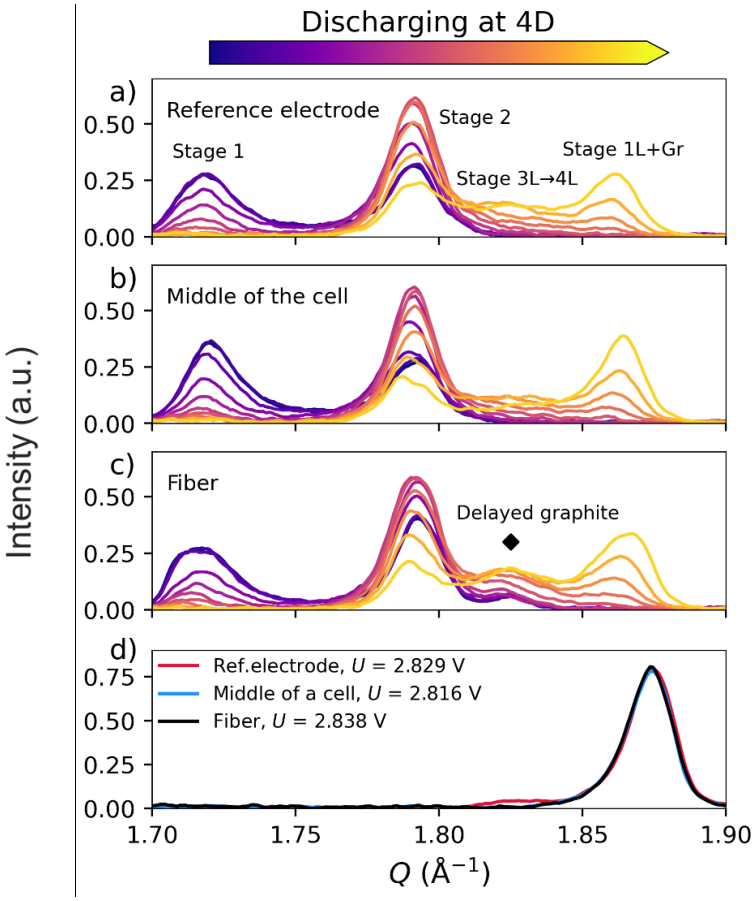

Figure 12. Diffraction patterns were collected during fast discharging **a)** near the reference electrode, **b)** middle of the cell, **c)** near the optical fiber, and **d)** from all the positions in a fully delithiated state after residual discharging.

3.4 Further Discussion

In this study, a temperature-sensitive optical fiber was integrated into a commercial multi-layered cell to measure temperature changes inside the multi-layered cell. Observations made in this work can offer valuable guidance for improving the accuracy of sensors with a similar design.

In general, only a single sensor/optical fiber is embedded into a lithium-ion battery cell to measure key parameters [56–58]. This may not be an issue when temperature is measured, however, based on the results presented in this work, uncertainties should be considered while correlating measured parameters with a state of charge or a lithiation degree of the graphite electrode. For instance, Ghannoum *et al.* employed a single optical fiber to measure strain in a lithium-ion battery pouch cell and correlated localized strain changes with the state of lithiation of the graphite electrode [57]. Nonetheless, Nascimento *et al.* demonstrated that strain values exhibit significant variations across different regions within a cell, highlighting that locally measured data may not accurately represent the entire cell [59].

This work supports that one should be critical when correlating locally measured parameters (e.g., strain) with Li-ions concentration, state of lithiation, or charge. In this study, delayed graphite was detected around the optical fiber throughout the charging process, resulting in a heterogeneous lithiation degree within the cell. It is fair to assume that the size of an optical fiber plays an important role in the degree of deformed electrodes around the optical fiber and, therefore, the formation of the delayed graphite.

One way to lower the amount of delayed graphite around the optical fiber could be by reducing the diameter of the optical fiber. Notably, a considerably thinner reference electrode exhibited no delayed graphite compared to the optical fiber.

Another approach could be to gain insight into deformed electrode layers around an optical fiber. Computed tomography could shed light on local deformations caused by an optical fiber. Computed tomography has been mainly used to study deformations in cylindrical jelly roll lithium-ion battery cells, and very few studies have explored the impact of an optical fiber on prismatic pouch cells. By understanding the deformations caused by an optical fiber, it is possible to model differences in lithiation kinetics around the optical fiber and the rest of the cell. This enables a more accurate estimation of the state of charge and increases the safety of a battery.

Summary

This work focused on studying two fully operational electrochemical cells – a single-layer cell and a commercial multi-layered pouch cell equipped with a reference electrode and temperature-sensitive optical fiber, by analysing the data obtained from *operando* wide-angle X-ray scattering (WAXS) experiments. The WAXS experiments were conducted on the BM02 beamline in the European Synchrotron (ESRF) as a part of the INSTABAT project.

The study aimed to provide insight into the impact of the temperature-sensitive sensor (optical fiber) on the lithiation kinetics and whether the data obtained near the optical fiber accurately represents the entire cell or exclusively the region around the optical fiber. The first part of the work aimed to validate the behaviour of the single-layer cell to use it as a reference point to study the impact of the configuration and geometry of the multi-layered cell on the lithiation kinetics within the graphite electrode. Compared to the single-layer cell, the multi-layered cell demonstrated lagged graphite lithiation. The lagged lithiation was probably caused by the outer graphite electrode regions not facing the positive electrode.

The optical fiber had a considerable impact on the lithiation kinetics, resulting in the formation of localized delayed graphite. The delayed graphite around the optical fiber was observed throughout the charging at C/5 and 2C. While charging at C/5, the delayed graphite finally caught up with the normal graphite at the end of the hold step, and no significant differences in the state of charge were observed between areas near the optical fiber and in the middle of the multi-layered cell. However, the delayed graphite became more prominent when the cell was charged at a higher C-rate of 2C and stayed present even at the end of the hold step applied after charging.

In conclusion, the study demonstrated that the presence of an optical fiber affects the lithiation of some regions and, hence, localized heterogeneities in the lithiation state around the optical fiber. It was assumed that the insertion of an optical fiber might have deformed the electrode layers and possibly increased the distance between electrodes around the optical fiber, resulting in a heterogeneous state of charge within the multi-layered cell throughout charging at various C-rates. These results demonstrate that the information on the state of charge obtained near the optical fiber exclusively describes the region around the optical fiber.

Kokkuvõte

Käesolevas töös analüüsiti grafiitelektroodi struktuurimuutusi kahes liitiumioonakus – monokihilises ja kommertsiaalses mitmekihilises liitiumioonakus. Akude karakteriseerimiseks kasutati *operando* WAXS meetodit Euroopa sünkrotronkiirguse uurimise keskuses BM02 kiirekanalil. Eksperiment viidi läbi INSTABAT projekti raames, mille eesmärgiks on arendada välja niinimetatud nutikas liitiumioonaku, kuhu lisatud sensorid võimaldavad saada informatsiooni aku seisukorra kohta reaalajas.

Töö esimeses osas uuriti struktuurimuutusi ja Li_xC_6 faaside tekkimist monokihilise aku grafiitelektroodis täis- ja tühjakslaadimise ajal erinevatel voolutihedustel. Saadud tulemusi kasutati võrdluspunktina, et mõista, kuidas mõjutab kommetrsiaalse aku mitmekihiline elektroodide konfiguratsioon Li-ioonide kineetikat ja Li_xC_6 faaside tekkimist. Monokihilise ja kommetrsiaalse aku difraktogrammide võrdlemisel valitud potentsiaalidel selgus, et spetsiifilise konfiguratsiooni tõttu on Li_xC_6 faaside moodustumine kommertsiaalses akus aeglasem ja heterogeennsem kui monokihilises akus.

Töö teises osas uuriti optilise fiibri mõju Li-ioonide kineetikale ja Li_xC_6 faaside moodustumisele. Difraktogrammid, mis koguti optilise fiibri juurest, näitasid, et lisaks oodatud Li_xC_6 faasidele kindlatel potentsiaalilel, on grafiitelektroodis alad, kus Li-ioonide kontsentratsioon on madalam. Madalal voolutihedusel laadides, Li-ioonide kontsentratsioon optilise fiibri ümber ühtlustus täislaadimise lõpuks. Lisaks ei täheldatud täislaetud olekus erisusi Li-ioonide kontsentratsioonis grafiitelektroodis optilise fiibri läheduses ja aku keskel. Selgus, et voolutiheduse tõstmisel muutus Li-ioonide kontsentratsioon grafiitelektroodis optilise fiibri ümber heterogeensemaks. Erinevalt madalal voolutihedusel laadimisest, olid isegi täislaetud olekus optilise fiibri ümber alad, kus Li-ioonide kontsentratsioon oli madalam. Seetõttu ei olnud ka enam Li-ioonide kontsentratsioon optilise fiibri ümber ja aku keskel võrreldavad.

Saadud tulemuste põhjal võib järeldada, et optilise fiibri sisestamine kommertsiaalsesse akusse mõjutab lokaalset Li-ioonide kineetikat ja sellest tulenevalt ka Li_xC_6 faaside moodustumist. Võib eeldada, et optilise fiibri tõttu suurendavad elektroodi kihtide vahekaugused optilise fiibri ümber ja elektroodikihtide geomeetria on deformeerunud, võrreldes muude aladega akus. Sellest tulenevalt võib väita, et optiline fiiber annab informatsiooni ainult lokaalsete parameetrite kohta täis- ja tühjakslaadimise vältel.

Acknowledgments

I would like to express my deepest gratitude to my supervisors, Sandrine Lyonnard, Quentin Jacquet, and Rasmus Palm, for their interesting discussions, patience, and invaluable feedback. I learned a lot from all the challenges I faced. I am also grateful to the STEP group at CEA (especially Ove Korjus, Quentin Berrod, and Federico Monaco) for supporting me on my journey. Working with and being guided by such innovative people has been a pleasure.

I would like to sincerely thank all the researchers who conducted the operando WAXS experiments at ESRF. The data analysed in this thesis was collected during the *operando* wide-angle X-ray scattering experiments conducted during the collaboration of INSTABAT and BIGMAP projects. The projects have received funding from the European Union's Horizon 2020 research and innovation program under grant agreement No. 955930. INSTABAT project carried out in the framework of the BATTERY 2030+ large-scale initiative funded by the European Union's Horizon 2020 research and innovation program under grant agreement No. 957213.

Finally, on a more personal note, I would like to thank all my friends who supported me in the past two years. Without them, I wouldn't have dared to go and study abroad. Sometimes, drinking coffee after lunch ends up in unexpected ways.

References

1. M. Li, J. Lu, Z. Chen, K. Amine, 30 Years of Lithium-Ion Batteries, Adv. Mater. 30 (2018) 1800561.
2. M. Brudermüller, B. Sobotka, D. Waughray, A Vision for a Sustainable Battery Value Chain in 2030 Unlocking the Full Potential to Power Sustainable Development and Climate Change Mitigation, World Economic Forum, Switzerland, 2019.
3. Communication from The Commission to The European Parliament, The European Council, The Council, The European Economic and Social Committee and The Committee of The Regions, European Commission, Brussels, 2019.
4. H. Ritchie, M. Roser, P. Rosado, Renewable Energy, https://ourworldindata.org/renewable-energy. Accessed 16/08/2023
5. O. Raccurt, The INSTABAT Project Presentation, Instabat. https://www.instabat.eu/instabat-development-project-presentation/. Accessed 16/08/2023
6. A. Fotouhi, K. Propp, D.J. Auger, S. Longo, State of Charge and State of Health Estimation Over the Battery Lifespan, in: G. Pistoia, B. Liaw (Eds.), Behav. Lithium-Ion Batter. Electr. Veh. Battery Health Perform. Saf. Cost, Springer International Publishing, Cham, (2018) pp. 267–288.
7. J.A. Braun, R. Behmann, D. Schmider, W.G. Bessler, State of charge and state of health diagnosis of batteries with voltage-controlled models, J. Power Sources. 544 (2022) 231828.
8. S. Petrovic, Battery Technology Crash Course: A Concise Introduction, Springer International Publishing, Cham, 2021, Happy Valley, pp. 4, 5, 29, 95, 97.
9. V.S. Bagotsky, Electrochemical Power Sources, John Wiley & Sons, Inc, Hoboken, New Jersey , 2015, pp. 5, 75, 77.
10. Z. Yang, J. Zhang, M.C.W. Kintner-Meyer, X. Lu, D. Choi, J.P. Lemmon, J. Liu, Electrochemical Energy Storage for Green Grid, Chem. Rev. 111 (2011) 3577–3613.11. T. Prohaska, J. Irrgeher, J. Benefield, J.K. Böhlke, L.A. Chesson, T.B. Coplen, T. Ding, P.J.H. Dunn, M. Gröning, N.E. Holden, H.A.J. Meijer, H. Moossen, A. Possolo, Y. Takahashi, J. Vogl, T. Walczyk, J. Wang, M.E. Wieser, S. Yoneda, X.-K. Zhu, J. Meija, Standard atomic weights of the elements 2021 (IUPAC Technical Report), Pure Appl. Chem. 94 (2022) 573–600.
12. K. Mizushima, P.C. Jones, P.J. Wiseman, J.B. Goodenough, LixCoO2 (0, Mater. Res. Bull. 15 (1980) 783–789.

13. A. Yoshino, Development of Lithium Ion Battery, Mol. Cryst. Liq. Cryst. Sci. Technol. Sect. Mol. Cryst. Liq. Cryst. 340 (2000) 425–429.
14. A. Friesen, F. Horsthemke, X. Mönnighoff, G. Brunklaus, R. Krafft, M. Börner, T. Risthaus, M. Winter, F.M. Schappacher, Impact of cycling at low temperatures on the safety behavior of 18650-type lithium ion cells: Combined study of mechanical and thermal abuse testing accompanied by post-mortem analysis, J. Power Sources. 334 (2016) 1–11.
15. S. Shahid, M. Agelin-Chaab, A review of thermal runaway prevention and mitigation strategies for lithium-ion batteries, Energy Convers. Manag. X. 16 (2022) 100310.
16. X. Zeng, G.-L. Xu, Y. Li, X. Luo, F. Maglia, C. Bauer, S.F. Lux, O. Paschos, S.-J. Kim, P. Lamp, J. Lu, K. Amine, Z. Chen, Kinetic Study of Parasitic Reactions in Lithium-Ion Batteries: A Case Study on LiNi0.6Mn0.2Co0.2O2, ACS Appl. Mater. Interfaces. 8 (2016) 3446–3451.
17. S. Wang, K. Rafiz, J. Liu, Y. Jin, J.Y. S. Lin, Effects of lithium dendrites on thermal runaway and gassing of LiFePO 4 batteries, Sustain. Energy Fuels. 4 (2020) 2342–2351.
18. S. Mahmud, M. Rahman, M. Kamruzzaman, M.O. Ali, M.S.A. Emon, H. Khatun, M.R. Ali, Recent advances in lithium-ion battery materials for improved electrochemical performance: A review, Results Eng. 15 (2022) 100472.
19. H. Cavers, P. Molaiyan, M. Abdollahifar, U. Lassi, A. Kwade, Perspectives on Improving the Safety and Sustainability of High Voltage Lithium-Ion Batteries Through the Electrolyte and Separator Region, Adv. Energy Mater. 12 (2022) 2200147.
20. J. Huang, S.T. Boles, JM. Tarascon, Sensing as the key to battery lifetime and sustainability. *Nat Sustain* **5**, 194–204 (2022).,
21. J. Amici, P. Asinari, E. Ayerbe, P. Barboux, P. Bayle-Guillemaud, R.J. Behm, M. Berecibar, E. Berg, A. Bhowmik, S. Bodoardo, I.E. Castelli, I. Cekic-Laskovic, R. Christensen, S. Clark, R. Diehm, R. Dominko, M. Fichtner, A.A. Franco, A. Grimaud, N. Guillet, M. Hahlin, S. Hartmann, V. Heiries, K. Hermansson, A. Heuer, S. Jana, L. Jabbour, J. Kallo, A. Latz, H. Lorrmann, O.M. Løvvik, S. Lyonnard, M. Meeus, E. Paillard, S. Perraud, T. Placke, C. Punckt, O. Raccurt, J. Ruhland, E. Sheridan, H. Stein, J.-M. Tarascon, V. Trapp, T. Vegge, M. Weil, W. Wenzel, M. Winter, A. Wolf, K. Edström, A Roadmap for Transforming Research to Invent the Batteries of the Future Designed within the European Large Scale Research Initiative BATTERY 2030+, Adv. Energy Mater. 12 (2022) 2102785.
22. Sensing, https://battery2030.eu/research/research-areas/sensing/, Accessed 26/07/2023

23. H. Zhang, Y. Yang, D. Ren, L. Wang, X. He, Graphite as anode materials: Fundamental mechanism, recent progress and advances, Energy Storage Mater. 36 (2021) 147–170.
24. V. Gold, ed., The IUPAC Compendium of Chemical Terminology: The Gold Book, 4th ed., International Union of Pure and Applied Chemistry (IUPAC), Research Triangle Park, NC, 2019.
25. Y.W. Yap, N. Mahmed, M.N. Norizan, S.Z. Abd Rahim, M.N. Ahmad Salimi, K. Abdul Razak, I.S. Mohamad, M.M.A.-B. Abdullah, M.Y. Mohamad Yunus, Recent Advances in Synthesis of Graphite from Agricultural Bio-Waste Material: A Review, Materials. 16 (2023) 3601.
26. J. Asenbauer, T. Eisenmann, M. Kuenzel, A. Kazzazi, Z. Chen, D. Bresser, The success story of graphite as a lithium-ion anode material – fundamentals, remaining challenges, and recent developments including silicon (oxide) composites, Sustain. Energy Fuels. 4 (2020) 5387–5416.
27. H. Zhao, F. Yang, C. Li, T. Li, S. Zhang, C. Wang, Z. Zhang, R. Wang, Progress and perspectives on two-dimensional silicon anodes for lithium-ion batteries, ChemPhysMater. 2 (2023) 1–19.
28. P.U. Nzereogu, A.D. Omah, F.I. Ezema, E.I. Iwuoha, A.C. Nwanya, Anode materials for lithium-ion batteries: A review, Appl. Surf. Sci. Adv. 9 (2022) 100233.
29. S. Schweidler, L. de Biasi, A. Schiele, P. Hartmann, T. Brezesinski, J. Janek, Volume Changes of Graphite Anodes Revisited: A Combined Operando X-ray Diffraction and In Situ Pressure Analysis Study, J. Phys. Chem. C. 122 (2018) 8829–8835.
30. S. Konar, U. Häusserman, G. Svensson, Intercalation Compounds from LiH and Graphite: Relative Stability of Metastable Stages and Thermodynamic Stability of Dilute Stage Id, Chem. Mater. 27 (2015) 2566–2575.
31. J.R. Dahn, Phase diagram of Li x C 6, Phys. Rev. B. 44 (1991) 9170–9177.
32. Q. Liu, S. Li, S. Wang, X. Zhang, S. Zhou, Y. Bai, J. Zheng, X. Lu, Kinetically Determined Phase Transition from Stage II (LiC12) to Stage I (LiC6) in a Graphite Anode for Li-Ion Batteries, J. Phys. Chem. Lett. 9 (2018) 5567–5573.
33. C. Didier, W.K. Pang, Z. Guo, S. Schmid, V.K. Peterson, Phase Evolution and Intermittent Disorder in Electrochemically Lithiated Graphite Determined Using in Operando Neutron Diffraction, Chem. Mater. 32 (2020) 2518–2531.
34. S. Taminato, M. Yonemura, S. Shiotani, T. Kamiyama, S. Torii, M. Nagao, Y. Ishikawa, K. Mori, T. Fukunaga, Y. Onodera, T. Naka, M. Morishima, Y. Ukyo, D.S. Adipranoto, H. Arai, Y. Uchimoto, Z. Ogumi, K. Suzuki, M. Hirayama, R. Kanno, Real-time

observations of lithium battery reactions—operando neutron diffraction analysis during practical operation, Sci. Rep. 6 (2016) 28843.

35. A.A. Banaciu, E.G. Udristioiu, H.Y. Aboul-Enein, X-RAY DIFFRACTION: Instrumentation and Applications, Crit. Rev. Anal. Chem. 45 (2015) 289–299.
36. Y. Waseda, E. Matsubara, K. Shinoda, X-Ray Diffraction Crystallography: Introduction, Examples and Solved Problems, Springer Berlin Heidelberg, Berlin, Heidelberg, 2011.
37. Powder diffraction, Nat. Rev. Methods Primer. 1 (2021) 78.
38. F. Lin, Y. Liu, X. Yu, L. Cheng, A. Singer, O.G. Shpyrko, H.L. Xin, N. Tamura, C. Tian, T.-C. Weng, X.-Q. Yang, Y.S. Meng, D. Nordlund, W. Yang, M.M. Doeff, Synchrotron X-ray Analytical Techniques for Studying Materials Electrochemistry in Rechargeable Batteries, Chem. Rev. 117 (2017) 13123–13186.
39. A.P. Black, A. Sorrentino, F. Fauth, I. Yousef, L. Simonelli, C. Frontera, A. Ponrouch, D. Tonti, M.R. Palacín, Synchrotron radiation based *operando* characterization of battery materials, Chem. Sci. 14 (2023) 1641–1665.
40. S.-M. Bak, Z. Shadike, R. Lin, X. Yu, X.-Q. Yang, In situ/operando synchrotron-based X-ray techniques for lithium-ion battery research, NPG Asia Mater. 10 (2018) 563–580.
41. H. Charalambous, D.P. Abraham, A.R. Dunlop, S.E. Trask, A.N. Jansen, T.R. Tanim, P.R. Chinnam, A.M. Colclasure, W. Xu, A.A. Yakovenko, O.J. Borkiewicz, L.C. Gallington, U. Ruett, K.M. Wiaderek, Y. Ren, Revealing causes of macroscale heterogeneity in lithium ion pouch cells via synchrotron X-ray diffraction, J. Power Sources. 507 (2021) 230253.
42. A.P. Black, A. Sorrentino, F. Fauth, I. Yousef, L. Simonelli, C. Frontera, A. Ponrouch, D. Tonti, M.R. Palacín, Synchrotron radiation based *operando* characterization of battery materials, Chem. Sci. 14 (2023) 1641–1665.
43. S. Tardif, N. Dufour, J.-F. Colin, G. Gébel, M. Burghammer, A. Johannes, S. Lyonnard, M. Chandesris, Combining operando X-ray experiments and modelling to understand the heterogeneous lithiation of graphite electrodes, J. Mater. Chem. A. 9 (2021) 4281–4290.
44. P.S. Singh, Small-Angle Scattering Techniques (SAXS/SANS), in: Membr. Charact., Elsevier, 2017: pp. 95–111.
45. B. wu, Y. Yang, D. Liu, C. Niu, M. Gross, L. Seymour, H. Lee, P. Le, T. Vo, Z. Deng, E. Dufek, M. Whittingham, W. Liu, J. Xiao, Good Practices for Rechargeable Lithium Metal Batteries, J. Electrochem. Soc. 166 (2019) A4141–A4149.
46. H.L. Andersen, L. Djuandhi, U. Mittal, N. Sharma, Strategies for the Analysis of Graphite Electrode Function, Adv. Energy Mater. 11 (2021) 2102693.

47. C. Schmitt, A. Kube, N. Wagner, K.A. Friedrich, Understanding the Influence of Temperature on Phase Evolution during Lithium-Graphite (De-)Intercalation Processes: An Operando X-ray Diffraction Study, ChemElectroChem. 9 (2022) e202101342.
48. A.S. Leach, A.V. Llewellyn, C. Xu, C. Tan, T.M.M. Heenan, A. Dimitrijevic, K. Kleiner, C.P. Grey, D.J.L. Brett, C.C. Tang, P.R. Shearing, R. Jervis, Spatially Resolved Operando Synchrotron-Based X-Ray Diffraction Measurements of Ni-Rich Cathodes for Li-Ion Batteries, Front. Chem. Eng. 3 (2022) 794194.
49. C.K. Christensen, M.A. Karlsen, A.Ø. Drejer, B.P. Andersen, C.L. Jakobsen, M. Johansen, D.R. Sørensen, I. Kantor, M.R.V. Jørgensen, D.B. Ravnsbæk, Beam damage in operando X-ray diffraction studies of Li-ion batteries, J. Synchrotron Radiat. 30 (2023) 561–570.
50. T. Coffey, S.G. Urquhart, H. Ade, Characterization of the effects of soft X-ray irradiation on polymers, J. Electron Spectrosc. Relat. Phenom. 122 (2002) 65–78.
51. T. Jousseaume, J.-F. Colin, M. Chandesris, S. Lyonnard, S. Tardif, How beam damage can skew synchrotron operando studies of batteries, Chemistry, 2023.
52. T. Bond, R. Gauthier, A. Eldesoky, J. Harlow, J.R. Dahn, In Situ Imaging of Electrode Thickness Growth and Electrolyte Depletion in Single-Crystal vs Polycrystalline LiNixMnyCozO2/Graphite Pouch Cells using Multi-Scale Computed Tomography, J. Electrochem. Soc. 169 (2022) 020501.
53. M.K.G. Bauer, J.R. Dahn, Using Lithium-ion Differential Thermal Analysis to Probe Tortuosity of Negative Electrodes in Lithium-Ion Cells, J. Electrochem. Soc. 168 (2021) 020501.
54. J. Wilhelm, S. Seidlmayer, P. Keil, J. Schuster, A. Kriele, R. Gilles, A. Jossen, Cycling capacity recovery effect: A coulombic efficiency and post-mortem study, J. Power Sources. 365 (2017) 327–338.
55. M. Hess, T. Sasaki, C. Villevieille, P. Novák, Combined operando X-ray diffraction–electrochemical impedance spectroscopy detecting solid solution reactions of LiFePO4 in batteries, Nat. Commun. 6 (2015) 8169.
56. C.-J. Bae, A. Manandhar, P. Kiesel, A. Raghavan, Monitoring the Strain Evolution of Lithium-Ion Battery Electrodes using an Optical Fiber Bragg Grating Sensor, Energy Technol. 4 (2016) 851–855.
57. A. Ghannoum, P. Nieva, Graphite lithiation and capacity fade monitoring of lithium ion batteries using optical fibers, J. Energy Storage. 28 (2020) 101233.

58. C. Gardner, E. Langhammer, W. Du, D.J.L. Brett, P.R. Shearing, A.J. Roberts, T. Amietszajew, In-Situ Li-Ion Pouch Cell Diagnostics Utilising Plasmonic Based Optical Fibre Sensors, Sensors. 22 (2022) 738.
59. M. Nascimento, S. Novais, M.S. Ding, M.S. Ferreira, S. Koch, S. Passerini, J.L. Pinto, Internal strain and temperature discrimination with optical fiber hybrid sensors in Li-ion batteries, J. Power Sources. 410–411 (2019) 1–9.

Appendix A. Characteristics of The Single-Layer Cell and The Commercial Multi-Layered Prismatic Pouch Cell

Appendix A1. The single-layer cell components (casing, electrodes, separator, current collectors, electrolyte) and their properties.

Single-layer cell			
	Material	**Thickness (µm)**	**Geometrical area (cm^2)**
Casing	Polypropylene/Al/Polyamide		80
Positive electrode	$LiNi_{0.6}Mn_{0.2}Co_{0.2}O_2$ (NMC622)	55	10.24
Positive electrode current collector (CC)	Al	12	10.24
Separator	Polyethylene + one-side coated with Al2O3	15	16
Negative electrode	Artificial graphite	52	12.25
Current collector	Cu	8	12.25
Electrolyte	1M $LiPF_6$ EC-EMC (3:7 volume%) + 2 mass% VC		

Appendix A2. Multi-layered cell components (casing, electrodes, separator, current collectors, electrolyte) and their properties. *Inner side of the electrode, **outer side of the electrode, and ***total coating area.

	Material	**Thickness (µm)**	**Dimensions**
Casing	Polypropylene/Al/Polyamide	106	162.5 x 213 cm
Positive electrode material	$LiNi_{0.6}Mn_{0.2}Co_{0.2}O_2$ (NMC622)	55	42.5 x 5.8 cm* 32.7 x 5.8 cm** 436.74 cm^2***
CC	Al	12	x
Positive electrode	NMC622 + Al + NMC622	122	595.6 cm^2
Separator	Polyethylene + one-side coated with Al_2O_3	15	x
Negative electrode material	Commercial graphite	52	33.9 x 6 cm* 43 x 6 cm** 461.4 cm^2**
CC	Cu	8	x
Negative electrode	Graphite + Cu + Graphite	112	511.6 cm^2
Electrolyte	1M $LiPF_6$ EC-EMC (3:7 volume%) + 2 mass% VC		

Appendix A3. The multi-layered cell's characteristics.

Positive electrode	Electrode material	NMC622
	Active material loading (wt%)	96.4
	Active material loading (mg cm^{-2})	16.7
	Areal capacity (mAh cm^{-2})	2.8
Negative electrode	Electrode material	Commercial graphite
	Active material loading (wt%)	94.8
	Active material loading (mg cm^{-2})	10
	Areal capacity (mAh cm^{-2})	x
Multi-layered cell	Practical capacity (Ah)	1.1
	Average voltage (at 0.2C) (V)	3.7
	Voltage range (V)	3.0–4.2
	Gravimetric energy density (Wh kg^{-1})	214
	Volumetric energy density (Wh L^{-1})	425

Appendix B. Designs of The Multi-Layered Cell, The Reference Electrode, and The Optical Fiber

Appendix B1. Dimensions (height and width) of the double-side coated negative electrode and the positive electrode. **a)** Coating width of the outer side of the graphite electrode (430 mm) and the inner side of the NMC622 electrode (426 mm). **b)** Coating width and height of the inner side of the graphite electrode (339 mm x 60 mm), and the outer side of the NMC622 electrode (327 mm x 58 mm). The total widths of the graphite electrode and the NMC622 electrode were 430 mm and 510 mm, respectively.

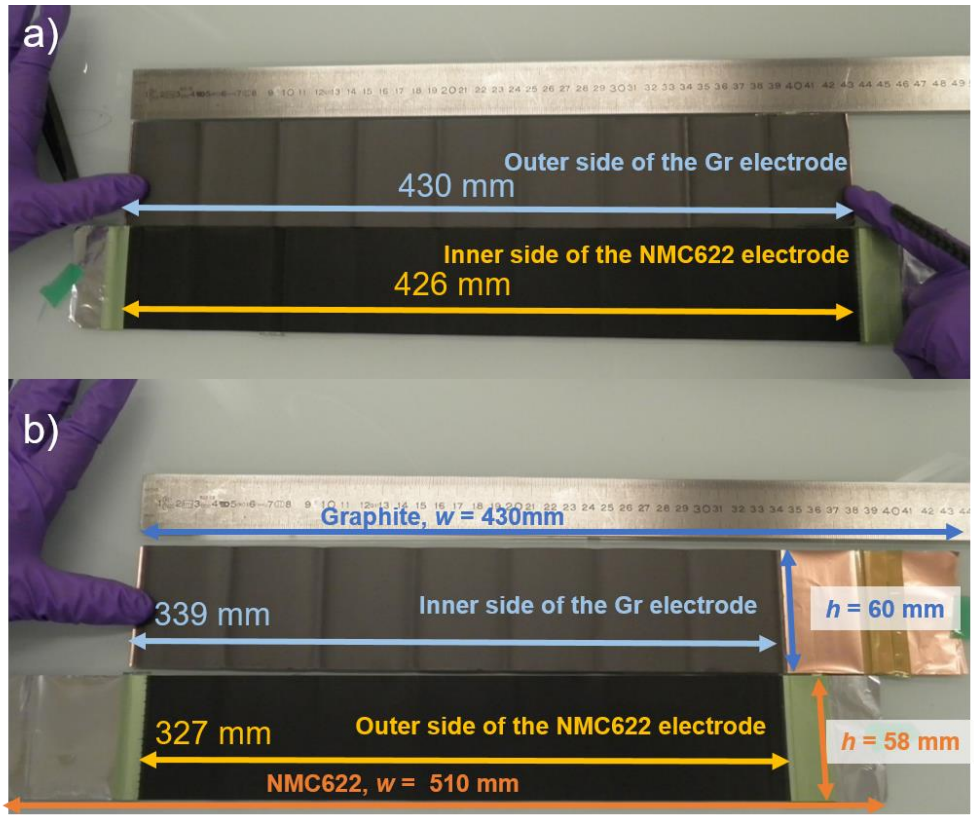

Appendix B2. **a)** Dry multi-layered prismatic pouch cell with a practical capacity of 1.1 Ah provided by Li-Fun Technology. **b)** Placement of the optical fiber and the reference electrode in the multi-layered prismatic pouch cell.

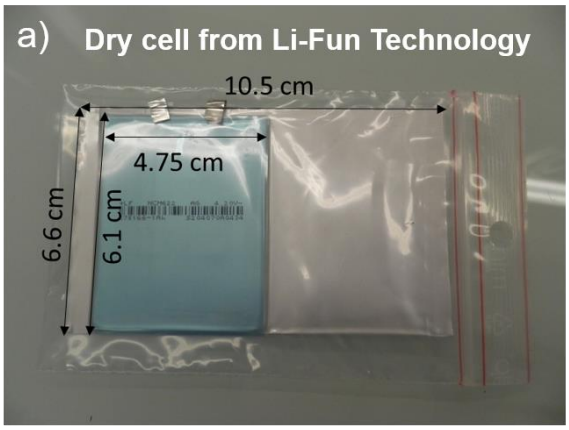

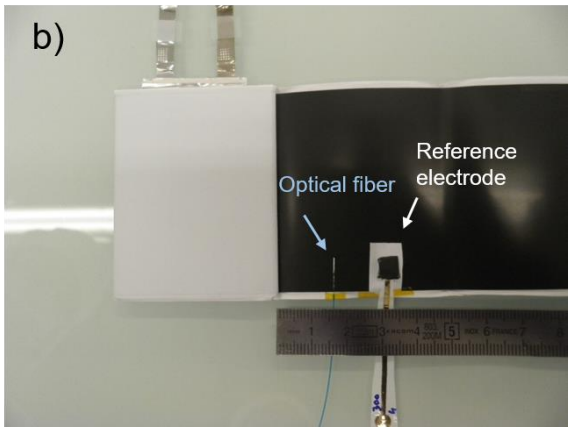

Appendix B3. Illustrative depiction and dimensions of a) the reference electrode and b) the optical fiber.

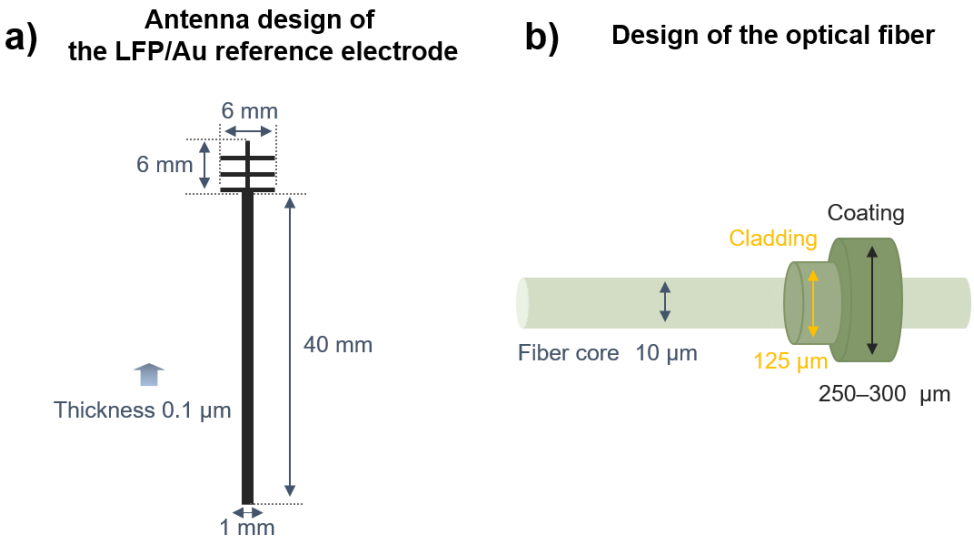

Appendix B4. The setup of the multi-layered prismatic pouch cell equipped with the reference electrode, the optical fiber, and seven thermocouples (TC) for the *operando* WAXS measurement. **a)** Back side of the multi-layered cell. Three holes with a diameter of 1 mm were drilled into the metal plate, one hole in the middle of the cell (blue), the second one near the reference electrode (pink), and the third one near the optical fiber (grey). **b)** Front side of the multi-layered cell and the placement of thermocouples.

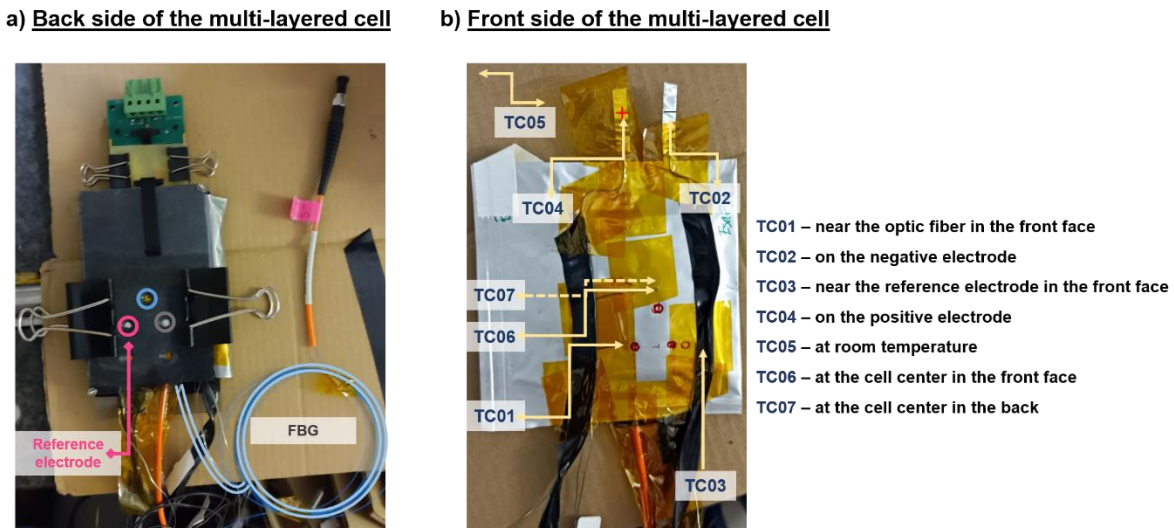

Appendix C. Galvanostatic Charging-Discharging Curves

Appendix C1. Galvanostatic charging-discharging cycling sequence of **a)** the single-layer cell and **b)** the multi-layered cell. After every charge at a C-rate of C, a hold step at U = 4.2 V was applied to stabilize the system. A standby step was added at the end of every discharge at a C-rate of D.

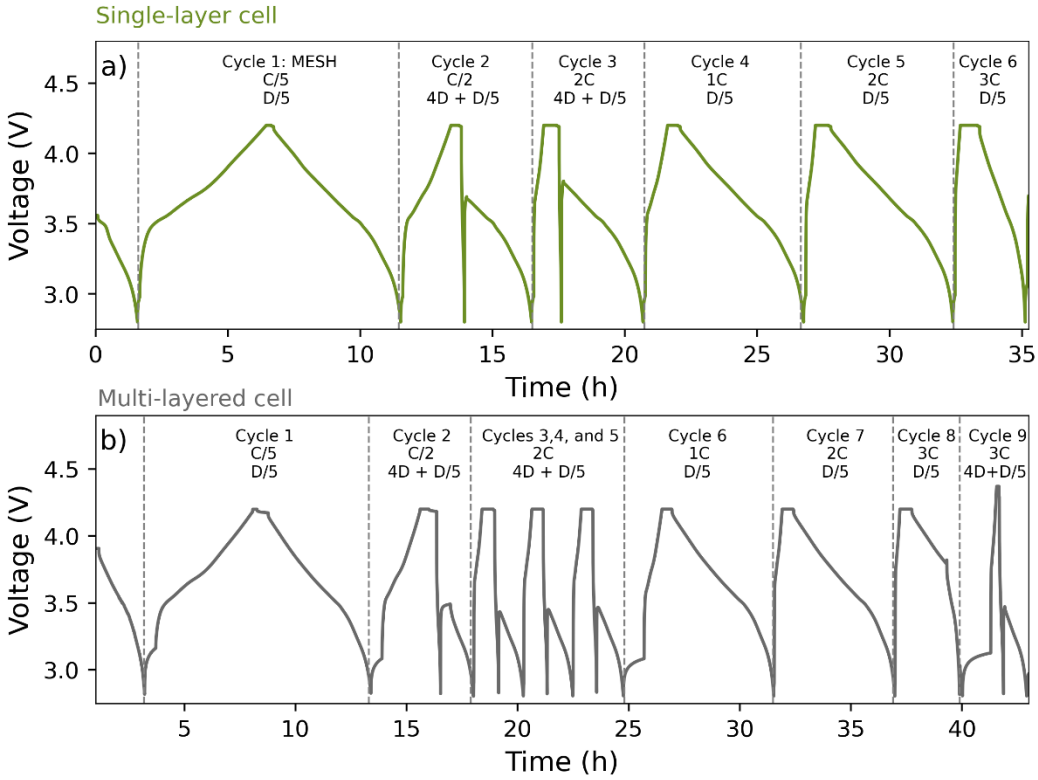

Appendix D. Positions of Different Scanning Points for The WAXS Experiments

Appendix D1. Selected scanning points and their positions for the single-layer cell measurement. The measurement started with the MESH, where nine different scanning points were scanned in the sequence of 3→2→1→6→5→4→9→8→7. The counting time (ct) per pattern at a scanning point was 30 seconds. After the MESH measurement, only the center of a hole (scanning point 5, ct = 15 seconds) and control point (ct = 1 second) were scanned.

Scanning point	**x-position**	**z-position**
Scanning point 3	117.95	30.25
Scanning point 2	117.45	30.25
Scanning point 1	116.95	30.25
Scanning point 6	117.95	30.75
Scanning point 5	117.45	30.75
Scanning point 4	116.95	30.75
Scanning point 9	117.95	31.25
Scanning point 8	117.45	31.25
Scanning point 7	116.95	31.25
Control point	117.25	30.75

Appendix D2. Selected scanning points and their positions for the multi-layered cell measurement. The measurement started with the MESH, where nine different scanning points were scanned in the sequence of 3→2→1→6→5→4→9→8→7. The counting time (ct) per pattern at a scanning point was 30 seconds. After the MESH measurement, the center of each hole (scanning point no. 5, ct = 15 seconds) was scanned.

Hole	**Reference electrode**		**Middle of the cell**		**Optical fiber**	
Scanning point	**x-position**	**z-position**	**x-position**	**z-position**	**x-position**	**z-position**
Scanning point 3	110.95	49.4	121.35	35.232	131.55	49.044
Scanning point 2	110.45	49.4	120.85	35.232	131.05	49.044
Scanning point 1	109.95	49.4	120.35	35.232	130.55	49.044
Scanning point 6	110.95	49.9	121.35	35.732	131.55	49.544
Scanning point 5	110.45	49.9	120.85	35.732	131.05	49.544
Scanning point 4	109.95	49.9	120.35	35.732	130.55	49.544
Scanning point 9	110.95	50.4	121.35	36.232	131.55	50.044
Scanning point 8	110.45	50.4	120.85	36.232	131.05	50.044
Scanning point 7	109.95	50.4	120.35	36.232	130.55	50.044

Appendix E. 2D Plots and Phase Fractions of The Single-Layer Cell and Beam Damage Evolution

Appendix E 1. a) Voltage (V) *vs*. Time (h) of the single-layer cell from, **b)** 2D plot of the continuously scanned point in the middle of the cell, and **c)** 2D plot of the collected patterns from the control point were obtained.

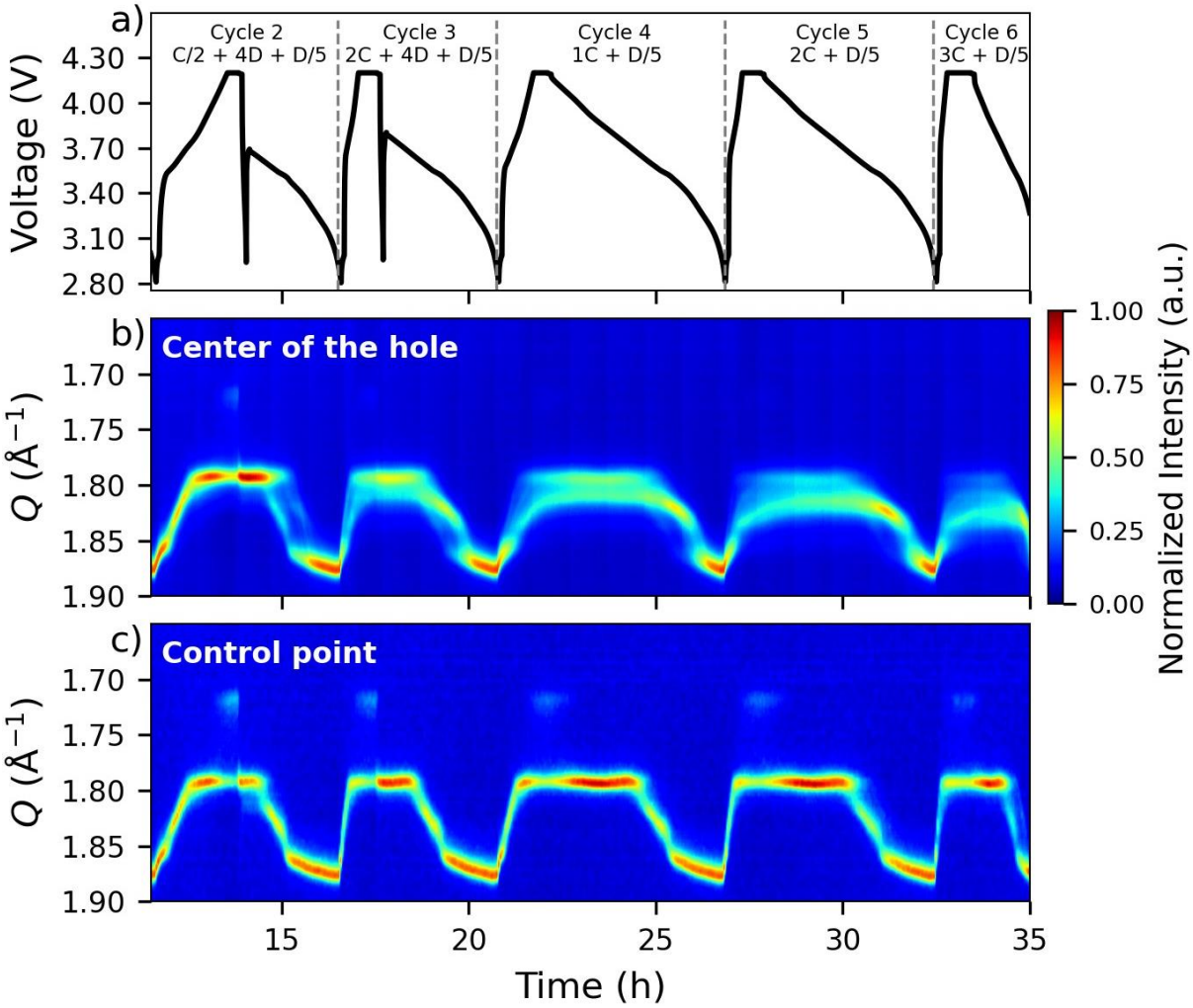

Appendix E2. Single-layer cell phase fractions obtained from diffraction patterns collected at the center of the hole (scanning point no. 5) while cycling the cell at various current rates of **a)** C/2+4D+D/5**, b)** 2C+4D+D/5, **c)** 1C+D/5, **d)** 2C+D/5, and **e)** 3C+D/5.

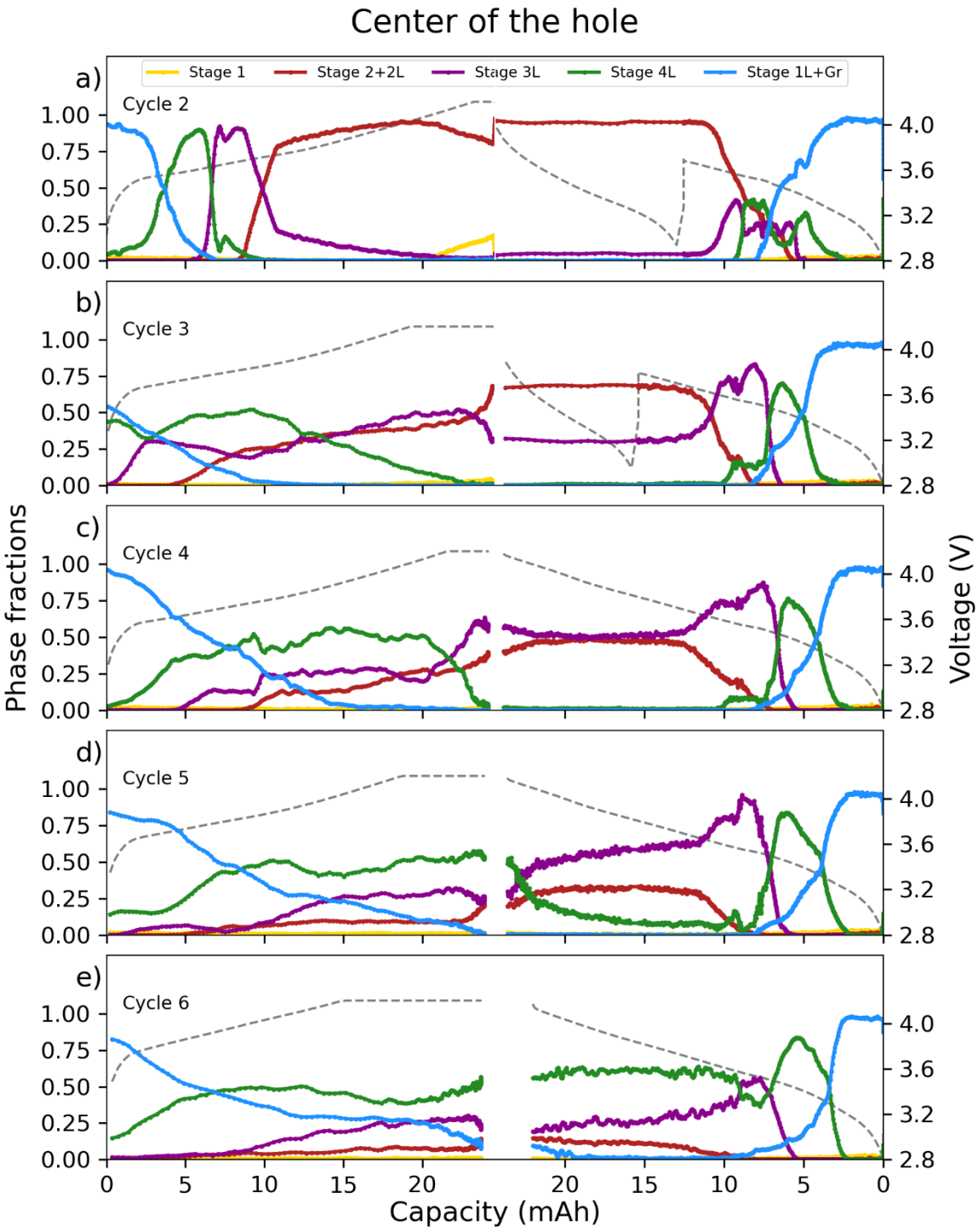

Appendix E3. Single-layer cell phase fractions obtained from diffraction patterns collected at the control point while cycling the cell at various current rates of **a)** C/2+4D+D/5**, b)** 2C+4D+D/5, **c)** 1C+D/5, **d)** 2C+D/5, and **e)** 3C+D/5.

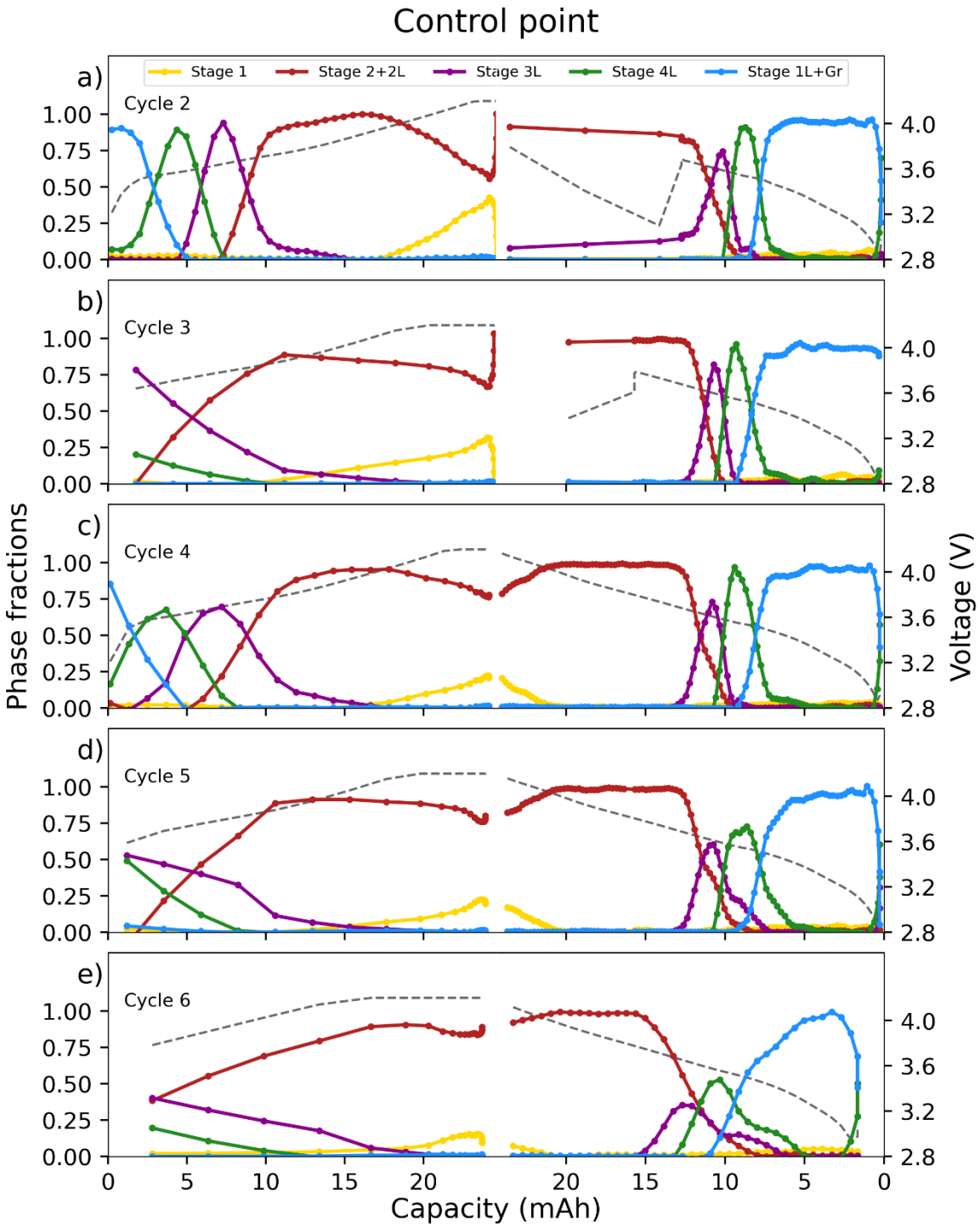

Appendix E4. Radiation dose (MGy) evolution in time (min) of **a)** the three first graphite electrode layers of the multi-layered cell and **b)** the single-layer cell graphite electrode.

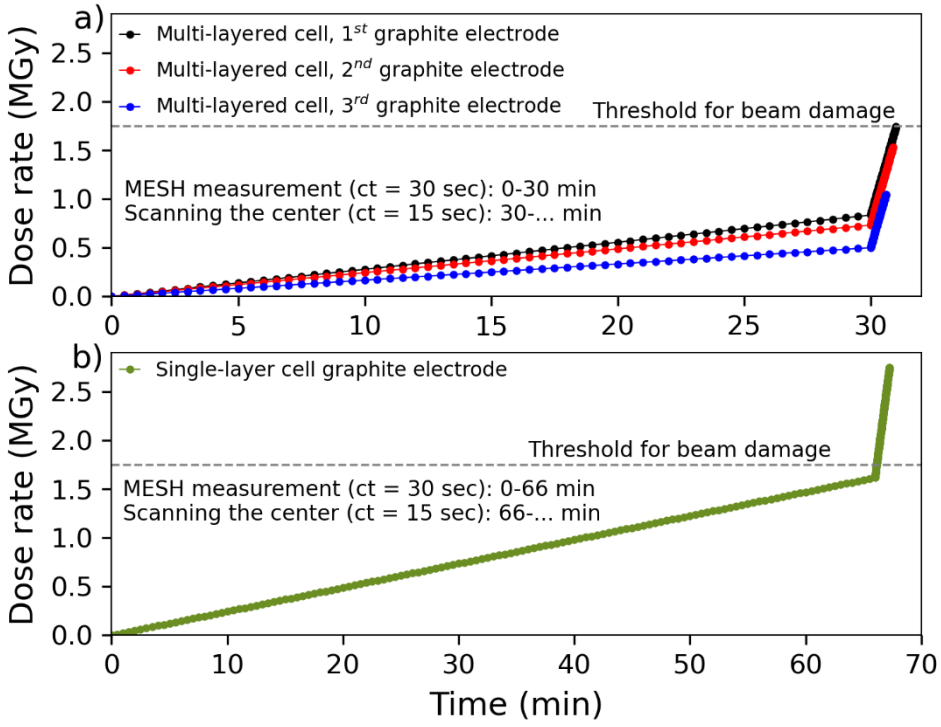

Appendix F. Diffraction Patterns of The Multi-Layered Cell

Appendix F1. Diffraction patterns were collected near the reference electrode, middle of the cell, and near the optical fiber during **a-f)** charging at C/5, and **g-l)** 2C. Delayed graphite in the optical fiber diffraction patterns is marked with ♦.

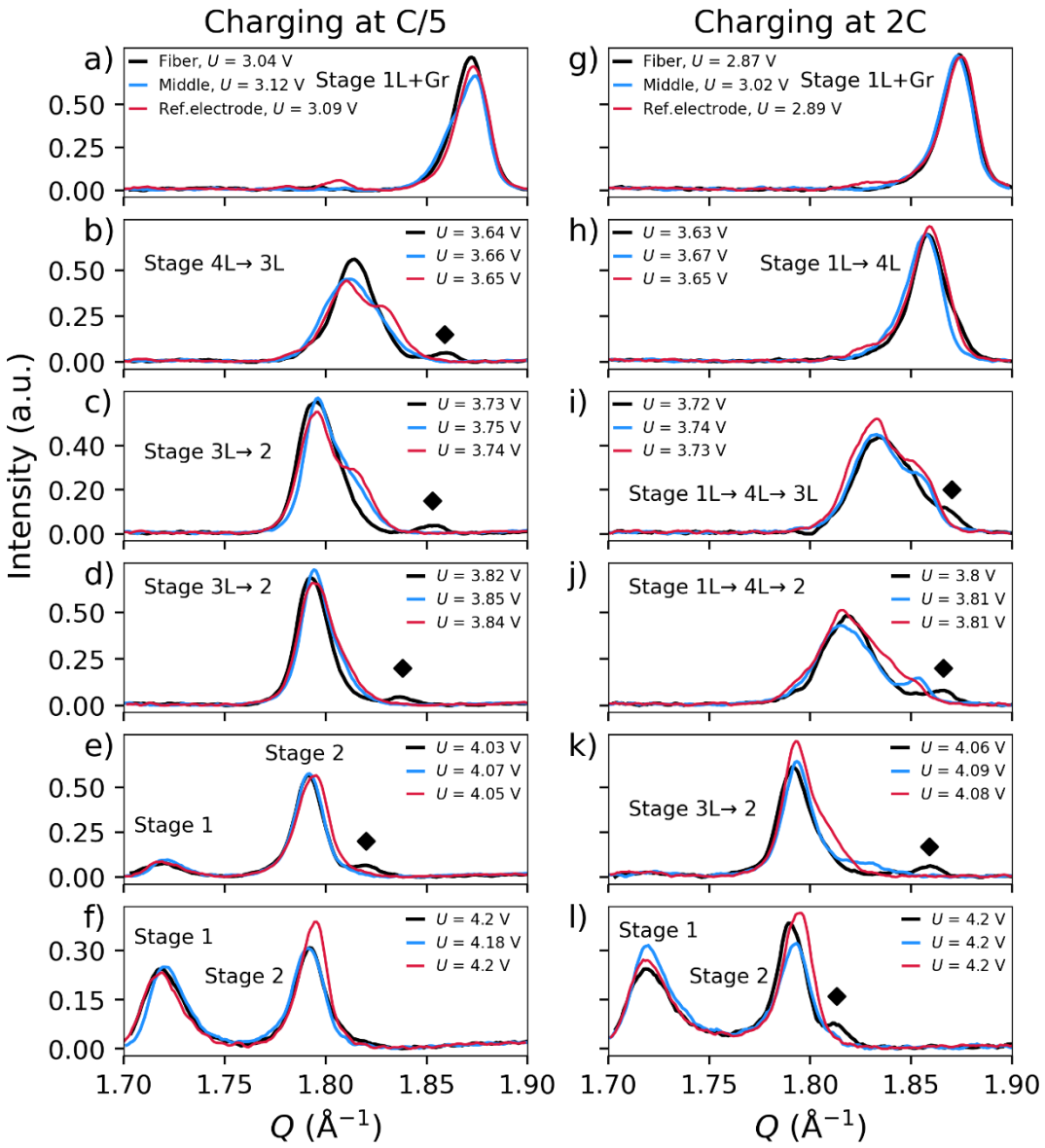

Non-exclusive licence to reproduce the thesis and make the thesis public

I, Annabel Olgo,

1. grant the University of Tartu a free permit (non-exclusive licence) to:

1.1 reproduce, for the purpose of preservation, including for adding to the DSpace digital archives until the expiry of the term of copyright, my thesis

The Impact of a Temperature-Sensitive Sensor on a Commercial Li-ion Battery Cell Graphite Electrode

Supervised by Dr Rasmus Palm, Dr Quentin Jacquet, and Dr Sandrine Lyonnard

2. I grant the University of Tartu the permit to make the thesis specified in point 1 available to the public via the web environment of the University of Tartu, including via the DSpace digital archives, under the Creative Commons licence CC BY NC ND 4.0, which allows, by giving appropriate credit to the author, to reproduce, distribute the work and communicate it to the public, and prohibits the creation of derivative works and any commercial use of the work from ***11/09/2025*** until the expiry of the term of copyright,

3. I am aware that the author retains the rights specified in points 1 and 2.

4. I confirm that granting the non-exclusive licence does not infringe other persons' intellectual property rights or rights arising from the personal data protection legislation.

.

Annabel Olgo

11/09/2023